Urban Climate 58 (2024) 102201

Contents lists available at ScienceDirect

Urban Climate

journal homepage: www.elsevier.com/locate/uclim

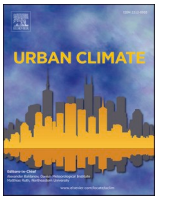

Contributions of temperature and humidity to intra-city variations in humid heat

Yichen Yang *, Xuhui Lee

School of the Environment, Yale University, 195 Prospect Street, New Haven, CT 06511, USA

ARTICLE INFO

Keywords:
Humid heat
Mobile measurement
Intra-city variation
Seasonal change
Built-up neighborhood

ABSTRACT

In this study, we investigated the intracity variation of humid heat in consideration of the contributions from temperature and humidity. Data were collected from mobile surveys in a mid-latitude industrial city. We found greater humid heat in built-up neighborhoods than in rural neighborhoods. Land surface temperature exaggerates the disparity in heat exposure as opposed to air temperature, although their spatial variations bear a strong resemblance. Humid heat is more variable across the city at night than during the day. Its nighttime variation is stronger in the cold season than in the warm season. Weather exerts a strong influence on the spatial variation in humid heat. The greatest variation was observed in the conditions of weak wind, low solar radiation, and high soil moisture in the day, and in the weak-wind and dry-soil conditions at night. The daytime humid heat increases in the built-up neighborhoods because these neighborhoods dissipate surface moist static energy less efficiently than the rural neighborhoods. The nighttime humid heat varies within the city mainly because the release of heat stored in the built-up neighborhoods is at a higher rate than the heat release from the rural soil.

1. Introduction

Urban population has grown rapidly in the past decades and is projected to reach 70 % of the world's population by 2050 (Economic, U. D. O., & Affairs, S., 2018). The well-being of urban residents is adversely affected by the urban heat island (UHI), the phenomenon characterized as elevated temperature in built-up land compared with the surrounding rural land. A large body of studies have examined the urban heat stress by comparing average conditions between urban (built-up) land and the adjacent rural land (Stewart, 2011). This two end-member comparison omits intra-city variations in characteristics like urban form and greenspace, and as a result the exposure of some urban residents to heat stress may be underestimated. It is imperative to examine the spatial variability of heat stress within a city in order to attain deeper insights into heat disparity across neighborhoods and to develop adaption strategies.

To date, studies on intra-city variations in heat stress are mostly based on the land surface temperature (LST) provided by satellite monitoring. Satellite LST is strongly dependent on urban land use type and morphological characteristics. Large LST differences have been observed between urban greenspaces (parks and gardens) and artificial surfaces without greenery (buildings, roads, and airports). Generally, LST decreases with increasing vegetation abundance due to cooling by plant transpiration. This temperature reduction depends on vegetation type, greenspace size, and greenspace shape (Yang et al., 2020b; Yu et al., 2017; Yu et al., 2018). In addition to vegetation, building morphology can also modify LST. In the daytime, neighborhoods with compact buildings may be cooler due to

* Corresponding author.
E-mail address: yichen.yang@yale.edu (Y. Yang).

https://doi.org/10.1016/j.uclim.2024.102201
Received 17 July 2024; Received in revised form 9 October 2024; Accepted 4 November 2024

greater shade provision than those with sparse buildings (Cilek and Cilek, 2021; Koc et al., 2018; Yu et al., 2019). On the other hand, greater building compactness may increase the nighttime LST because the street canyon traps more heat (Logan et al., 2020; Oke, 1981; Oke, 1982).

The presence of LST hot and cold spots in a city has motivated the assessment of heat exposure disparity among different demographic and socioeconomic groups. In the US, people of color and from low-income backgrounds experience higher LST than White and wealthier populations (Chakraborty et al., 2019; Chakraborty et al., 2023; Hsu et al., 2021). A limitation of these studies is that LST does not directly measure the heat stress experienced by human bodies. The LST can vary by more than 10 °C in a city (Daramola and Balogun, 2019; Kuang et al., 2015; Logan et al., 2020; Tran et al., 2017; Yang and Lee, 2022). However, intra-city variation in air temperature, which is a more appropriate measure of heat exposure, is much weaker. In one comparative study of the LST and air temperature, the LST difference between the coolest (an urban forest) and the warmest (a parking lot) land parcels along a street network was 11.3 °C (Yang and Lee, 2022). In comparison, the air temperature measured along the same network changed by only 1.5 °C. In another study, the spatial variation of the LST is greater than that of air temperature by a factor of 1.3 to 5.4 (Nichol and Wong, 2008). Use of the LST alone as the heat stress metric may exaggerate the actual heat exposure disparity.

Besides air temperature, air humidity is another determinant of heat stress. Because the human skin is more capable of dissipating heat via evaporation in drier conditions, an urban dry island (UDI), that is, lower humidity in built-up land than in rural land, will improve thermal comfort, having an opposite effect to the UHI (Zhang et al., 2023). But the urban moisture land (UMI), with higher humidity in built-up land than in rural land, will aggravate human heat stress. So far, only a few observational studies on intra-city variations in humidity have been published (Jonsson, 2004; Noro et al., 2015; Waugh et al., 2023; Yang et al., 2020a). It is not known if humidity variations are positively or negatively correlated spatially with temperature variations. Air humidity will intensify heat stress in high temperature neighborhoods if the correlation is positive and will reduce heat stress if the correlation is negative.

In this study, we aim to investigate the intra-city variations of humid heat in consideration of the relative importance of temperature and humidity changes. A smart sensor mounted on a passenger car was used to sample temperature and humidity variations. The mobile survey was repeated along a street network for 16 months. We used the wet-bulb temperature, calculated from the temperature and humidity data, as the measure of humid heat intensity. The data were used to address the following questions: (1) Which neighborhoods in the city are exposed to the greatest humid heat? (2) Do intracity variations in air temperature resemble variations in LST? (3) During which time of the day and season of the year does humid heat exhibit the greatest spatial variation? (4) What type of weather condition causes the greatest spatial variation in humid heat?

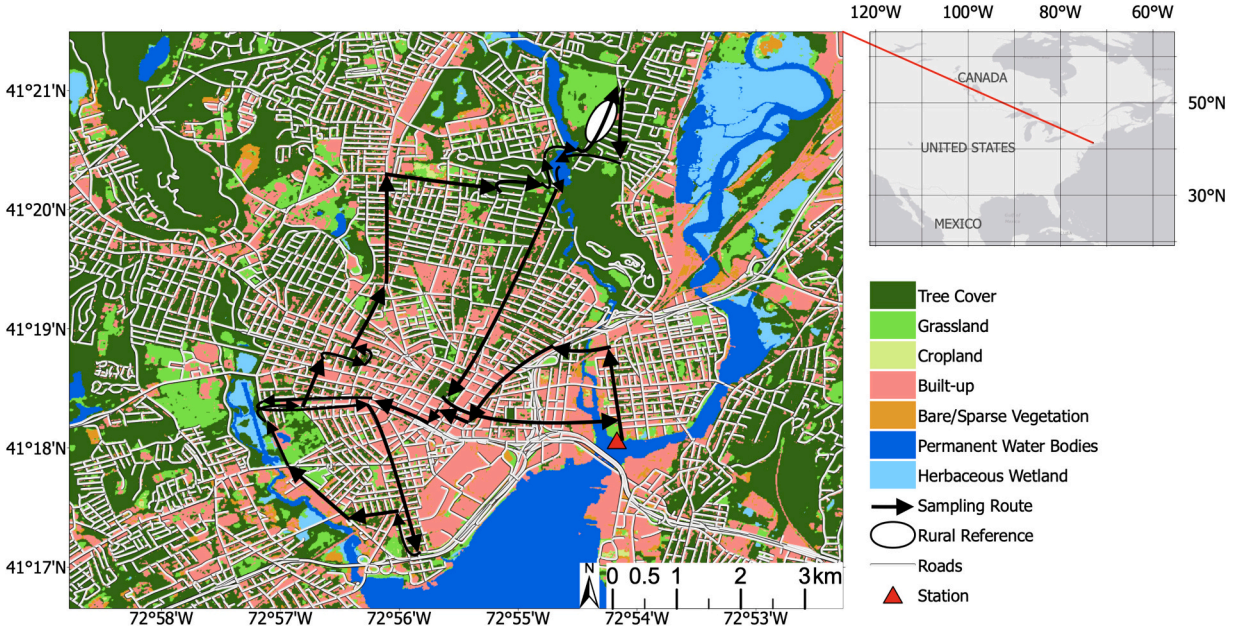

Fig. 1. Land cover map in the study area, New Haven, Connecticut, USA. Black lines indicate the sampling route, with arrows showing travel directions. White lines are road networks. The white ellipse is the rural reference. The red triangle indicates a NOAA weather station. Land cover data source: https://esa-worldcover.org/en. (For interpretation of the references to color in this figure legend, the reader is referred to the web version of this article.)

2. Materials and methods

2.1. Study area

Our study area is in the City of New Haven, Connecticut, the United States (Fig. 1). The city is located in the temperate Köppen climate zone (Köppen, 1900), with warm, humid summers and cold winters. The mean diurnal amplitude of temperature is about 7.5 °C. The monthly mean air temperature ranges from 0.1 °C to 23.7 °C, with an annual mean of 11.8 °C. The mean relative humidity is 73 % and the mean vapor pressure is 12 hPa. The annual precipitation is about 1030 mm. The total population was 135,307 of which 57.4 % are people of color based on the 2023 census data (https://data.census.gov/table?g=160XX00US0952000&y=2023). The city has a dense road network supporting busy transportation (thin white lines in Fig. 1). Its center is highly developed, and neighborhoods near its outskirt are densely vegetated lands.

2.2. Sensor and mobile measurement

Measurements were made with a smart temperature and humidity sensor (Smart-T) attached to the roof of a white passenger car (Supplementary Fig. 1). The approximate sampling height was 1.5 m above the ground. The Smart-T sensor is compact in size (85 mm tall), consisting of temperature and humidity sensing elements and a radiation shield. It uses the user's smart phone as data logging and geolocating device. The sensor performance has been extensively tested (Cao et al., 2020; Yang et al., 2024). A brief summary is provided here for the reader's convenience. A comparison between 30 sensor units and three commercial HOBO sensors (model MX2302A, Onset Computer Corporation, Bourne, Massachusetts, USA) was conducted in a well-ventilated room with stable temperature and humidity. Results show that the sensor's reproducibility or precision was 0.04 °C for temperature and 0.25 % for relative humidity. The mean bias (Smart-T minus HOBO) was −0.10 °C for temperature and + 3.4 % for relative humidity. In an outdoor test for comparison between a Smart-T sensor and a commercial fast-responding temperature-humidity sensor (6 mm diameter, model I-Met XQ2, InterMet Systems Inc., Grand Rapids, Michigan), Smart-T captured spatial variations in temperature and humidity similar to those of the I-Met sensor. The I-Met sensor was considered free from radiation interference due to its small thermocouple, which was protected by a ventilated sunlight shield. Compared to the I-Met sensor, the temperature radiation error of the Smart-T in full sunlight was less than 0.05 °C when the sensor is in motion. The user can choose a logging interval from 1 s to 60 s. In this study, the logging interval was set to 1 s, corresponding to 20 m of spatial resolution at a maximum vehicle speed of 20 m s^{-1}.

Each trip started near a NOAA weather station (red triangle, Fig. 1), traversed a network of pre-selected streets (black arrows, Fig. 1), and ended at the weather station. This sampling route was selected to maximize the urban-rural contrast in the landscape. The sampled locations represent land parcels ranging from totally pervious land to fully paved land. The trip length is about 40 km. The observation period was from October 2022 to January 2024, typically with one to two observational days per week. On each observation day, one trip was made during the daytime and one trip during the nighttime, except on August 2, 2023, when four trips were made (start time 10:00, 14:00, 19:00, and 22:00 local time). On August 2, the sky was clear, and the solar radiation was strong (exceeding 900 W m^{-2} at noon). There are a total of 109 day trips and 105 night trips. Most daytime trips (82 %) occurred between 11 AM and 4 PM local time, each lasting about 2 h. Most nighttime trips (91 %) occurred between 9 PM to 12 AM local time, each lasting about 1.5 h. There are 103 trips in the warm season (May to October, monthly mean temperature above 10 °C) and 111 trips in the cold season (November to April).

In Supplementary Fig. 2, we performed a 1:1 comparison of the Smart-T measurements against the NOAA station observations. In this comparison, the Smart-T measurements were made near the station at the beginning and the end of each trip. Results show excellent agreement ($R^2 > 0.97$, number of observations = 191).

2.3. Quantification of urban effects

We use the wet-bulb temperature (T_w) to represent the intensity of humid heat. The wet-bulb temperature T_w was calculated with the wet-bulb equation.

$$T_a - T_w = \frac{(e_w^* - e_a)}{\gamma} \tag{1}$$

where T_a is air temperature, e_a is vapor pressure, e_w^* denotes the saturation vapor pressure at T_w, and γ is the psychrometric constant. This equation was solved numerically from the observed T_a and e_a to obtain T_w at every sampling step.

The urban effects were quantified as spatial differences in air temperature (ΔT_a), vapor pressure (Δe_a) and the wet-bulb temperature (ΔT_w) between a given location on the measurement route and a heavily wooded reference neighborhood (white eclipse in Fig. 1) which belongs to the local climate zone (LCZ) class A (Dense Trees), based on a global LCZ product (Demuzere et al., 2022). The vapor pressure difference is divided by the psychrometric constant γ to give the temperature dimension (°C). Temporal trends in these variables during each measurement trip were removed using the stationary measurements at the NOAA weather station. We note that the spatial difference in the wet-bulb temperature (ΔT_w) is a linear combination of the temperature and the humidity differences (Zhang et al., 2023),

$$\Delta T_w = w_1 \Delta T_a + w_2 \frac{\Delta e_a}{\gamma} \tag{2}$$

where w_1 and w_2 are positive and dimensionless scaling factors given by

$$w_1 = w_2 = 1 \Big/ \left(1 + \frac{\Delta_w}{\gamma}\right) \tag{3}$$

with Δ_w denoting the slope of the saturation vapor pressure at T_w. Eq. (2) is obtained by spatial differentiation of Eq. (1). Its accuracy is better than 0.017 °C (Zhang et al., 2023).

We analyzed the data collected during individual trips as well ensemble means for all-season daytime, all-season nighttime, warm season daytime, warm season nighttime, cold season daytime, and cold season nighttime. To produce these ensemble mean spatial patterns, we discretized the sampling route into 611 segments, with each segment represented by a rectangle grid of 50 m (along the traveling direction) by 90 m (in the lateral direction). The grid mean ΔT_a, Δe_a and ΔT_w were first calculated for each trip using the data collected at the points that fall within the grid boundary and were then averaged across trips to obtain the ensemble mean values. Sampling grids with fewer than 5 overlapping trips were excluded from the ensemble results to enhance temporal representativeness. Maps of trip overlaps are provided in Supplementary Fig. 3.

2.4. Supporting data

To investigate weather impacts on humid heat, we acquired meteorological variables for the study area from ERA5-Land hourly reanalysis data, including solar radiation, wind speed at the height of 10 m, and soil moisture (surface soil layer water volume fraction). We obtained the LST data using Landsat 8 and 9 level 2 products. We used Impervious Surface Fraction (IMP) to represent the spatial variations in the degree of development. The IMP data was provided by the National Land Cover Database. Another landscape indicator was Normalized Difference Vegetation Index (NDVI), derived separately for the warm season and the cold season from the Sentinel-2 L2A satellite images. The LST data is at the 100-m spatial resolution. The IMP data at the 30-m resolution and the NDVI data at the 10-m resolution were resampled to 100-m resolution to enclose the size of the ensemble sampling grids. All the satellite images were acquired in the clear-sky conditions.

To investigate the mechanisms underlying the spatial patterns of urban humid heat, we used an empirical method to quantify urban roughness considering buildings and trees as the primary roughness elements. According to a previous study by (Grimmond and Oke, 1999) on urban roughness in global real cities, aerodynamic roughness can be modeled by the height and the plan areal fraction of roughness elements. Their relationship between z_0 (roughness length), H (height), and λ_p (plan areal fraction) can be approximated by (Supplementary Fig. 4)

$$z_0 = 12.6098 \times {\lambda_p}^{2.2} \times \left(1 - {\lambda_p}^5\right) \times \mathrm{H} \tag{4}$$

where λ_p is computed as the combined plan areal fraction of buildings (λ_{pb}) and trees (λ_{pt}),

$$\lambda_p = \lambda_{pb} + \lambda_{pt}(1 - p) \tag{5}$$

Here we include porosity of tree foliage (p), set to be 0.2 in the warm season and 0.6 in the cold season (Grimmond and Oke, 1999). The roughness element height (H) is the average height of buildings (H_b) and trees (H_t), weighted by plan area and with porosity considered for the trees:

$$\mathrm{H} = \frac{\lambda_{pb} H_b + \lambda_{pt}(1 - p) H_t}{\lambda_{pb} + \lambda_{pt}(1 - p)} \tag{6}$$

Here, λ_{pb} and H_b were obtained from the recently published GLAMOUR dataset at 100-m resolution (Li et al., 2024). Parameter λ_{pt} was computed, using the ESA WorldCover 2021 dataset, as the fraction of the original 10-m grids assigned the tree class within 100-m grids. Parameter H_t was derived from the Global Forest Canopy Height 2019 (Potapov et al., 2021) and aggregated from 30-m resolution to 100-m resolution. The computed z_0 was at 100-m resolution and then extracted within 150 m from each mobile sampling grid.

In addition, we computed building volume from the GLAMOUR dataset and conducted the same aggregation using the 150-m radius.

To assess heat disparity among communities, we used median household income as a proxy for their socioeconomic backgrounds, and percent of people of color to represent ethnic backgrounds. These two variables are at the census tract level, and were acquired from American Community Survey 2020. Their values were extracted by the sampling grids and then bin-averaged to reduce the uncertainty that occurred at the tract boundaries.

3. Results

3.1. All-season mean spatial variations

Built-up neighborhoods are generally warmer (Fig. 2a) and drier (Fig. 2b) than the rural reference during the day. For the five selected example neighborhoods (neighborhood 1–5 in Fig. 2b), they are all warmer than the rural reference, their ΔT_a ranging from 0.80 to 1.22 °C. In terms of the humidity difference, neighborhoods 1 and 2 experience large humidity reductions (1: $\Delta e_a/\gamma = -0.41$ °C; 2: $\Delta e_a/\gamma = -0.45$ °C). A weak humidity reduction is observed in neighborhood 3 ($\Delta e_a/\gamma = -0.16$ °C). The other two neighborhoods show almost no change in humidity (4: $\Delta e_a/\gamma = 0.01$ °C; 5: $\Delta e_a/\gamma = 0.00$ °C).

When temperature and humidity changes are combined, neighborhoods 3–5 show higher wet-bulb temperature or humid heat intensity than the rural reference during the daytime (ΔT_w from 0.47 °C to 0.61 °C; Fig. 2c). The T_w difference for neighborhoods 1 and 2 is weaker, i.e., $\Delta T_w = 0.25$°C and 0.17°C, respectively, because the contributions from humidity change and from temperature change have opposite signs and therefore offset each other. This offsetting effect is evident as a negative correlation between the temperature change and the humidity change across the city (Fig. 3a). According to Eq. 2, the black dashed line with the slope of − 1:1 in this figure indicates full compensation between temperature and humidity changes, that is, the temperature change is exactly canceled by the humidity change, leading to no change in the wet-bulb temperature. The parameter space above this line corresponds to positive ΔT_w and the space below it negative ΔT_w. The slope of linear regression of the actual data is − 0.69 (black solid line), showing that temperature change is only partially offset by humidity change, with the result being a net increase in humid heat relative to the rural reference neighborhood (Fig. 2c).

The nighttime spatial patterns differ from the daytime patterns in several respects. The city center (black circle in Fig. 4a) are both warmer (Fig. 4a) and more humid (Fig. 4b) than the rural reference neighborhood. In this area, the intensity of humid heat is enhanced by as much as 1.85 °C (Fig. 4c). The spatial correlation between ΔT_a and $\Delta e_a/\gamma$ is positive across the city with a positive regression slope of 0.30 (Fig. 3b). The majority of the datapoints lie above the full compensation line, or in other words, the increase in humid heat is contributed by increases in both temperature and humidity. Averaged across the whole street network, the nighttime ΔT_w is nearly doubled (0.73°C) in comparison to the daytime ΔT_w (0.30°C).

3.2. Comparison between air temperature and surface temperature

Fig. 5 is a comparison of the ensemble mean air temperature and the land surface temperature along the observational street network. The LST data is the ensemble average of 13 clear-sky Landsat 8 and Landsat 9 images spanning the entire measurement period. The acquisition time is approximately 10:30 local time. The LST variation (ΔLST) is presented as the LST of individual pixels minus the mean LST of the pixels in the rural reference neighborhood. Averaged throughout the year, LST is lower at the heavily wooded rural reference than in the built-up areas (Fig. 5b). Others LST cold spots correspond to urban parks, lawns, and waterbodies. A similar pattern is observed in the variations of air temperature (Fig. 5a). Supplementary Fig. 5 shows that air temperature is positively correlated with LST ($p < 0.01$), demonstrating resemblance between them. But the linear correlation was only 0.61, possibly due to the horizontal diffusion and advection in the atmosphere. The regression slope is 0.11, meaning that the variations in air temperature are only 11 % of the spatial variations in LST. In this city, LST exaggerates disparity of heat exposure by approximately ninefold.

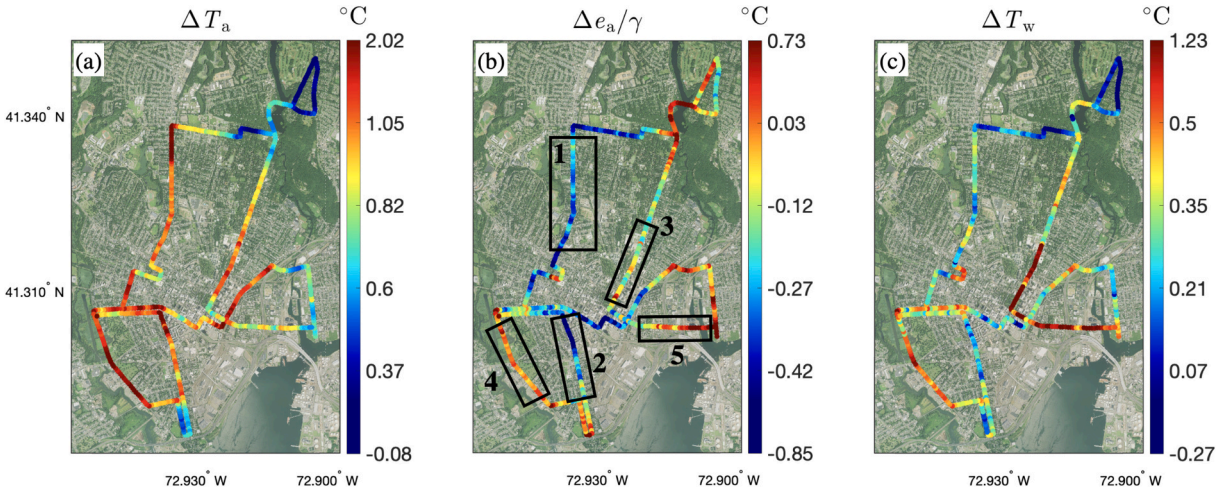

Fig. 2. Ensemble maps for daytime variations in (a) temperature, (b) humidity, and (c) wet-bulb temperature. Black boxes in (b) indicate five example neighborhoods. Background is a natural color satellite map.

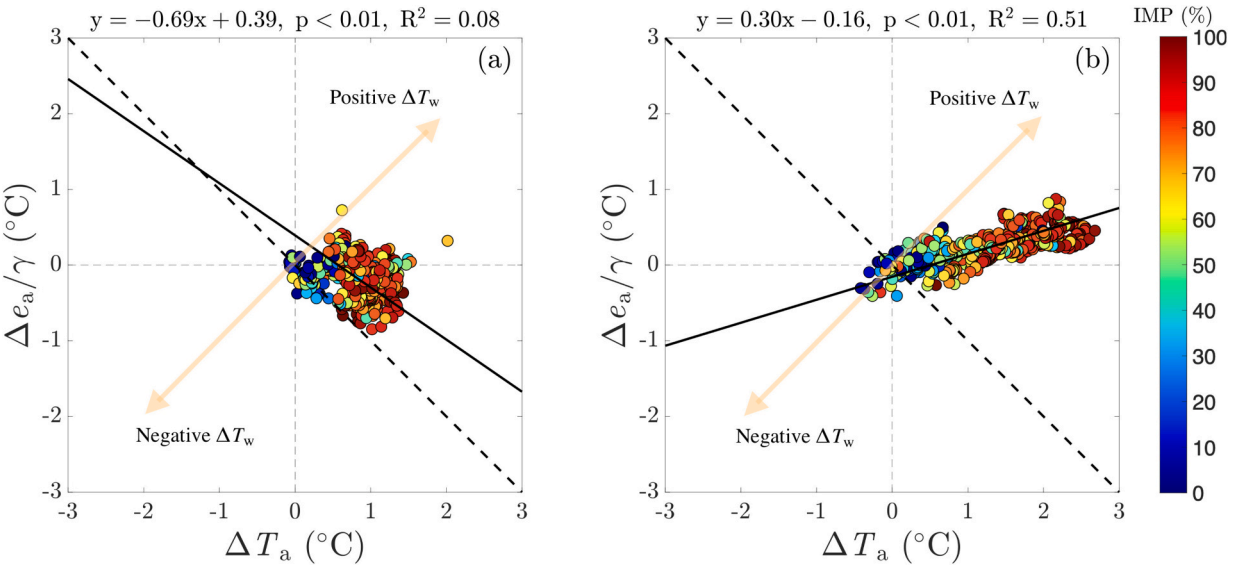

Fig. 3. Relationships between temperature change and humidity change in (a) daytime and (b) nighttime. Each data point represents a sampling grid. Color indicates impervious surface fraction. The black solid and dashed lines are best-fit function (with regression statistics shown) and the 1:1 relationship, respectively.

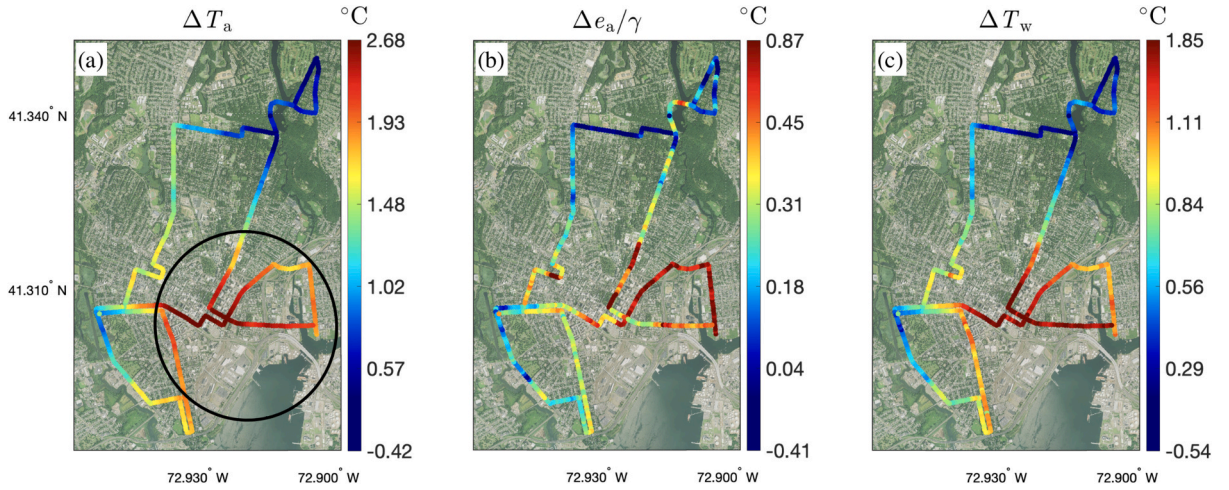

Fig. 4. Same as Fig. 2 but for nighttime variations. Circle in (a) marks the city center.

3.3. Spatial variations in the warm season and the cold season

Compared to the rural reference neighborhood, the daytime temperature in built-up neighborhoods is increased more in the warm season (mean $\Delta T_a = 1.09\ ^\circ$C; maximum $\Delta T_a = 3.02\ ^\circ$C; Supplementary Fig. 6a) than in the cold season (mean $\Delta T_a = 0.63\ ^\circ$C; maximum $\Delta T_a = 1.28\ ^\circ$C; Supplementary Fig. 6d). The daytime humidity varies more spatially in the warm season ($\Delta e_a/\gamma$ range from −1.33 to 1.77 °C) than in the cold season ($\Delta e_a/\gamma$ range from −0.54 to 0.10 °C). In the warm season, about half of the built-up grids in the daytime experienced decreased humidity and the rest increased humidity (Supplementary Fig. 6b). In the cold season, the daytime humidity in nearly all the built-up grids is lower than in the rural reference neighborhood (Supplementary Fig. 6e).

The nighttime temperature varies in similar ranges in the warm season (ΔT_a range from −0.42 to 2.71 °C; Supplementary Fig. 7a) and in the cold season (ΔT_a range from −0.42 to 2.51 °C; Supplementary Fig. 7d). On average, built-up neighborhoods are exposed to more increased temperature in the warm season (mean $\Delta T_a = 1.54\ ^\circ$C) than in the cold season (mean $\Delta T_a = 1.20\ ^\circ$C). The nighttime humidity is increased for the majority of built-up grids (92 %) in the warm season (mean $\Delta e_a/\gamma = 0.43\ ^\circ$C; maximum $\Delta e_a/\gamma = 1.81\ ^\circ$C; Supplementary Fig. 7b). In comparison, the cold-season shows attenuated variations in humidity ($\Delta e_a/\gamma$ range from −0.31 to 0.36 °C), with about 29 % grids showing negative $\Delta e_a/\gamma$ (Supplementary Fig. 7e).

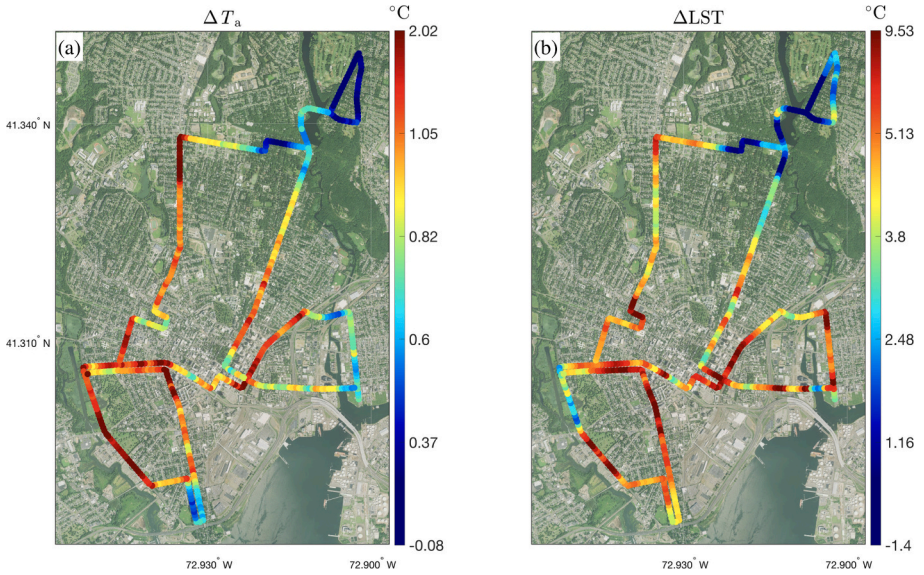

Fig. 5. Comparison of daytime variations in (a) air temperature and in (b) land surface temperature. The air temperature change is the all-season ensemble. The LST data is the ensemble average of 13 Landsat 8 and Landsat 9 images.

The positive daytime correlation and the negative nighttime correlation between $\Delta e_a/\gamma$ and ΔT_a are present in both the warm season and the cold season (Fig. 6). The change in the daytime wet-bulb temperature is similar between the warm season (mean $\Delta T_w = 0.31\ ^\circ C$; maximum $\Delta T_w = 1.26\ ^\circ C$; Supplementary Fig. 6c) and the cold season (mean $\Delta T_w = 0.27\ ^\circ C$; maximum $\Delta T_w = 1.08\ ^\circ C$;

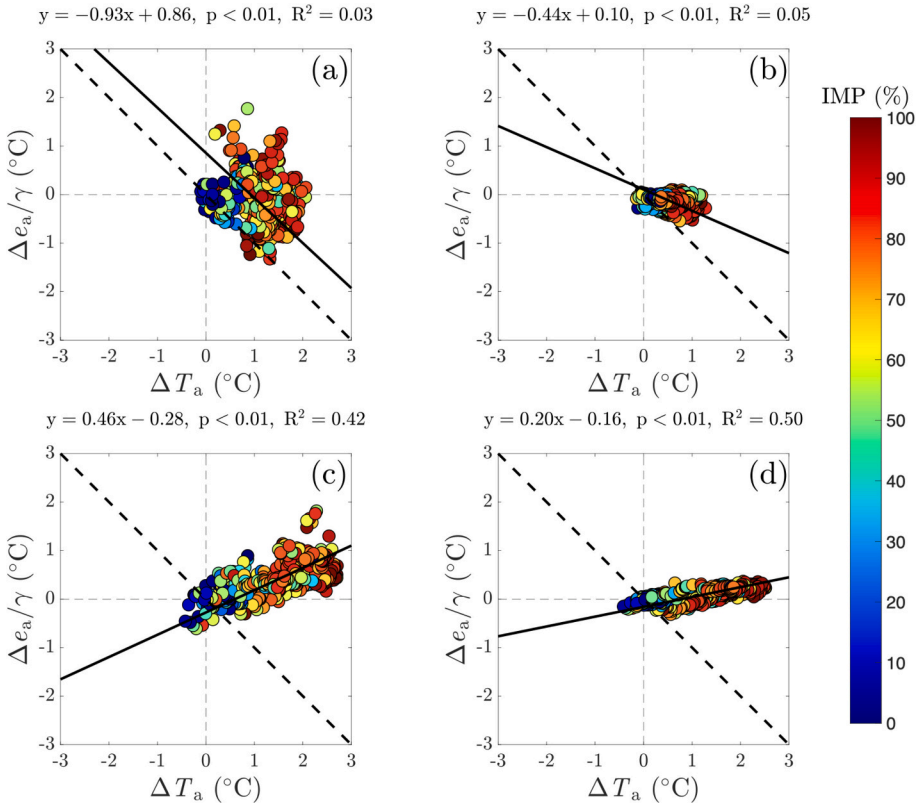

Fig. 6. Relationship between temperature and humidity variations a: warm season daytime; b: cold season daytime; c: warm season nighttime; d: cold season nighttime. Color indicates impervious surface fraction. The black solid and dashed lines are best-fit function (with regression statistics shown) and the − 1:1 relationship, respectively.

Supplementary Fig. 6f). The enhancement in the nighttime T_w in built-up neighborhoods is less in the warm season (mean$\Delta T_w = 0.68$ °C; maximum $\Delta T_w = 1.47$ °C; Supplementary Fig. 7c) than in the cold season (mean $\Delta T_w = 0.76$ °C; maximum $\Delta T_w = 1.78$ °C; Supplementary Fig. 7f).

3.4. Humid heat in highly built-up areas

Highly built-up areas are densely populated. We use IMP as a measure of the degree of development. In the following, we present the mean conditions of sampling grids with IMP greater than 90 %. The all-season mean T_w for these grids is increased by 0.38 °C in the day (Table 1). The increase in T_w at night (1.12 °C) is nearly three times greater than the increase in the day. This day-to-night contrast in these highly built-up grids is greater than for the entire city (Section 3.1). The stronger humid heat increase in the highly built-up grids is observed at night in the cold season ($\Delta T_w = 1.20$ °C; Table 1).

In all the temporal categories, temperature dominates over humidity in the intensification of humid heat in the highly built-up grids (Table 1). The temperature contribution ($w_1 \Delta T_a$) varies from 0.44 °C in daytime in the cold season to 1.08 °C at nighttime in the cold season. In comparison, the humidity contribution ($w_2 \Delta e_a/\gamma$) only varies between − 0.11 °C to 0.22n°C.

The diurnal measurement on August 2, 2023 (Fig. 7) confirms the dominant role of temperature in increasing humid heat in the early afternoon (2 PM) and late at night (10 PM). The morning (10 AM) and evening transitions (7 PM) are exceptions. At 10 AM, contributions of temperature ($w_1 \Delta T_a = 0.40$ °C) and humidity ($w_2 \Delta e_a/\gamma = -0.39$ °C) cancel each other, leading to almost no change in humid heat in the highly built-up neighborhoods. At 7 PM, these neighborhoods are exposed to large excess humid heat ($\Delta T_w = 1.27$ °C) owing to the positive contributions from both temperature ($w_1 \Delta T_a = 0.77$ °C) and humidity ($w_2 \Delta e_a/\gamma = 0.54$ °C).

3.5. Drivers of spatial variations in humid heat

Neighborhoods with high impervious surface fraction (IMP) tend to experience stronger humid heat. In the temperature versus humidity parameter space, sampling grids with greater IMP appear to deviate more in the positive direction from the full compensation line in both the warm and the cold season and the daytime and the nighttime. The same data presented as scatter plots reveals that ΔT_w increases linearly with IMP, from near zero values for the rural reference neighborhood (IMP = 0 %) to the greatest magnitude for fully developed grids (IMP = 100 %; Fig. 8). This statistical correlation is significant ($p < 0.01$) in both the daytime and the nighttime, and in the warm season and the cold season. The sensitivity to IMP is much greater at night than during the day. The daytime T_w is increased by 0.43 °C in the warm season and 0.39 °C in the cold season, and the nighttime T_w is increased by 1.01 °C in the warm season and 1.14 °C in the cold season, for a 100 % increase in IMP. In these figures, we also use the mean ΔT_w of sampling grids with IMP greater than 90 % to indicate the spatial variation (SV) of humid heat.

The correlation of ΔT_w with NDVI is negative (Supplementary Fig. 8). This is expected as NDVI and IMP are negatively correlated across space. The T_w sensitivity to NDVI is − 0.39 °C (warm season) and − 0.76 °C (cold season) in the daytime and − 1.62 °C (warm season) and − 3.63 °C (cold season) in the nighttime per unit NDVI increase.

The humid heat intensity differs markedly among local climate zones, suggesting urban morphology to be a driver of its spatial variations. Among the sampling grids outside the rural reference neighborhood (LCZ A: Dense Trees), the daytime humid heat is most intense in LCZ 8 (Large Low-rise) and the least in LCZ 6 (Open Low-rise). At night, the lowest humid heat intensity occurs in LCZ 6 and the highest in LCZ 10 (Heavy Industry). The LCZs were derived from a global LCZ product (Demuzere et al., 2022). This product was chosen over other LCZ products like the CONUS LCZ map (Demuzere et al., 2020) and maps from the LCZ generator (Demuzere et al., 2021) due to a high overall accuracy (~80 %) and a generalized model predictions based on most training samples.

3.6. Weather influence on spatial variations in humid heat

We consider three weather-related factors, solar radiation, soil moisture, and wind speed. For each weather factor, the trips are divided into two categories—high or low—depending on whether the factor during a particular trip is above or below the median value across all the trips. These median values are 373 W m^{-2} (solar radiation), 0.32 (soil moisture) and 3.0 m s^{-1} (wind speed). There are a total of 8 weather combinations or scenarios for daytime observations and four scenarios for nighttime observations. The number of trips in each combination ranges from 8 to 25. We then produced ensemble mean ΔT_a, $\Delta e_a/\gamma$ and ΔT_w of the highly built-up neighborhoods (81 sampling grids with IMP ≥ 90 %) for each scenario.

Table 1
Mean change in wet-bulb temperature (ΔT_w) in highly built-up grids (IMP >90 %), with the corresponding contributions from temperature ($w_1 \Delta T_a$) and humidity ($w_2 \Delta e_a/\gamma$). The scaling factors (w_1 and w_2) are given by Eq. 3, using the ensemble mean wet-bulb temperature at the rural reference grids.

	Daytime			Nighttime		
	ΔT_w (°C)	$w_1 \Delta T_a$ (°C)	$w_2 \Delta e_a/\gamma$ (°C)	ΔT_w (°C)	$w_1 \Delta T_a$ (°C)	$w_2 \Delta e_a/\gamma$ (°C)
Warm Season	0.35 (±0.22)	0.46 (±0.09)	−0.09 (±0.18)	0.96 (±0.21)	0.78 (±0.15)	0.22 (±0.11)
Cold Season	0.34 (±0.22)	0.44 (±0.11)	−0.11 (±0.07)	1.20 (±0.43)	1.08 (±0.31)	0.10 (±0.07)
All	0.38 (±0.24)	0.46 (±0.09)	−0.12 (±0.11)	1.12 (±0.35)	0.97 (±0.23)	0.18 (±0.09)

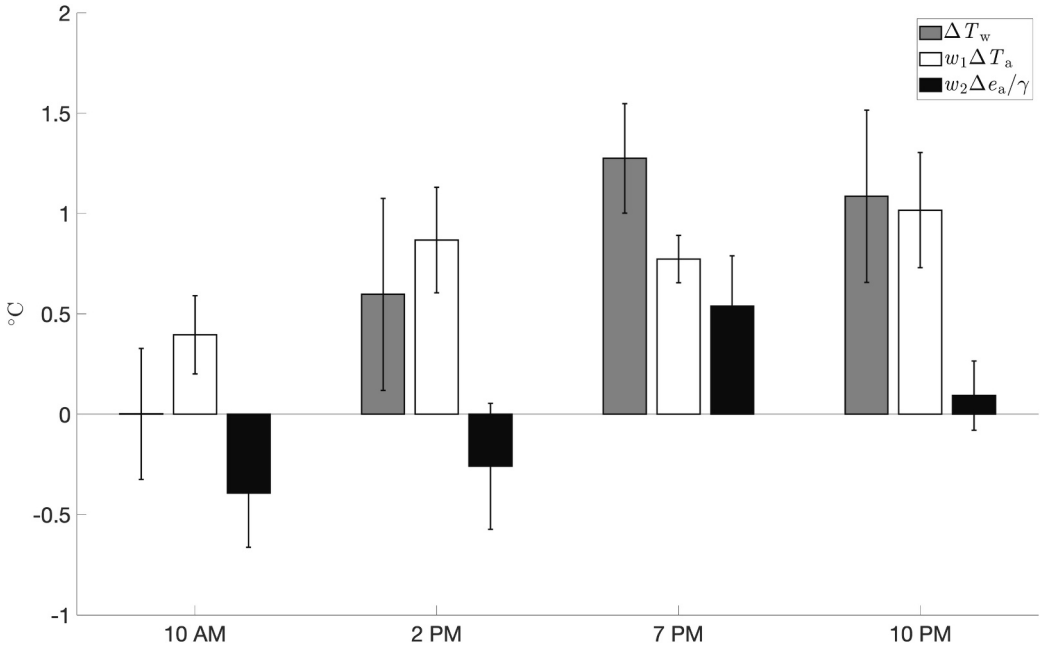

Fig. 7. Diurnal variations of change in wet-bulb temperature (ΔT_w) in highly built-up grids (IMP >90 %) on August 2, 2023. Contributions of temperature ($w_1 \Delta T_a$) and humidity ($w_2 \Delta e_a/\gamma$) are also shown. Error bars indicate ±1 standard deviation.

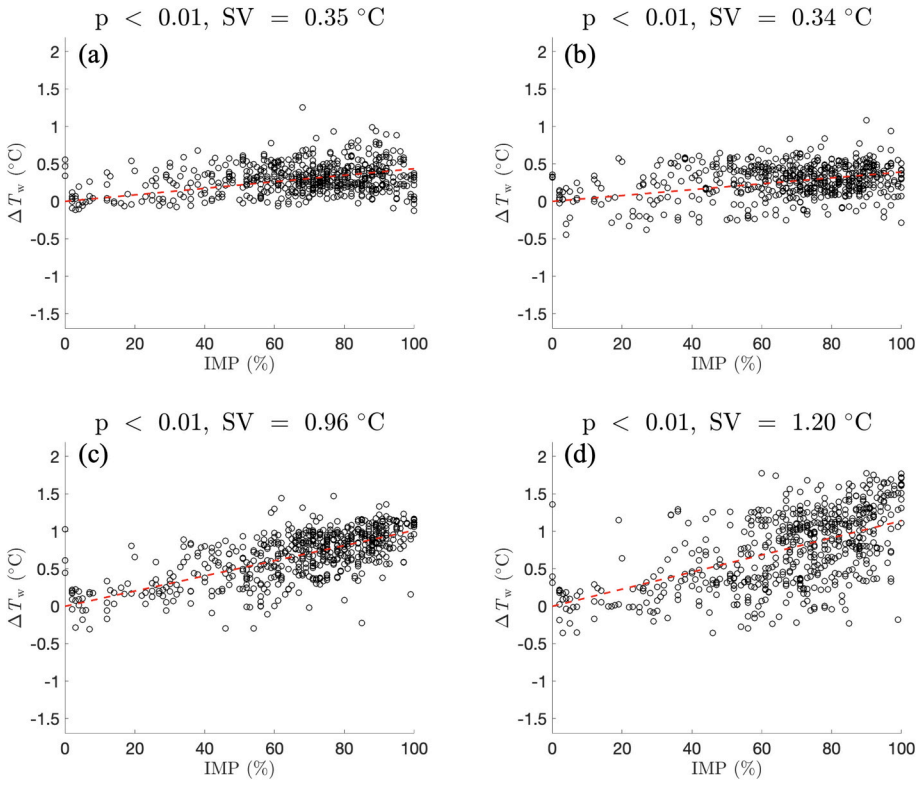

Fig. 8. Relationship between impervious surface fraction (IMP) and change in wet-bulb temperature (ΔT_w): (a) daytime in the warm season; (b) daytime in the cold season; (c) nighttime in the warm season; and (d) nighttime in the cold season. Red lines display the best-fitting functions. Each datapoint represents one sampling grid. Spatial variation (SV) is quantified as the mean ΔT_w of sampling grids with IMP greater than 90 %.

During the day, these highly built-up grids are warmer ($\Delta T_a > 0$) and drier ($\Delta e_a/\gamma < 0$) than the heavily wooded reference neighborhood in all the weather scenarios (Fig. 9a and b). Their mean wet-bulb temperature is greater than that in the rural reference neighborhood ($\Delta T_w > 0$) for seven of the eight weather scenarios. The temperature increase and the humidity reduction are more pronounced in weak wind than in strong wind due to increasing strength of atmospheric mixing with increasing wind speed. The greatest temperature increase occurs when wind speed is low, and solar radiation and soil moisture are high ($\Delta T_a = 1.82^{\circ}$C; Fig. 9a). This weather scenario also corresponds to the greatest reduction in humidity ($\Delta e_a/\gamma = -0.64^{\circ}$C; Fig. 9b). The largest increase in humid heat ($\Delta T_w = 0.61^{\circ}$C) is observed under the scenario of weak wind, low solar radiation and high soil moisture (Fig. 9c). Interestingly, under the scenario of strong wind, low solar radiation and low soil moisture, the T_w of these highly built-up

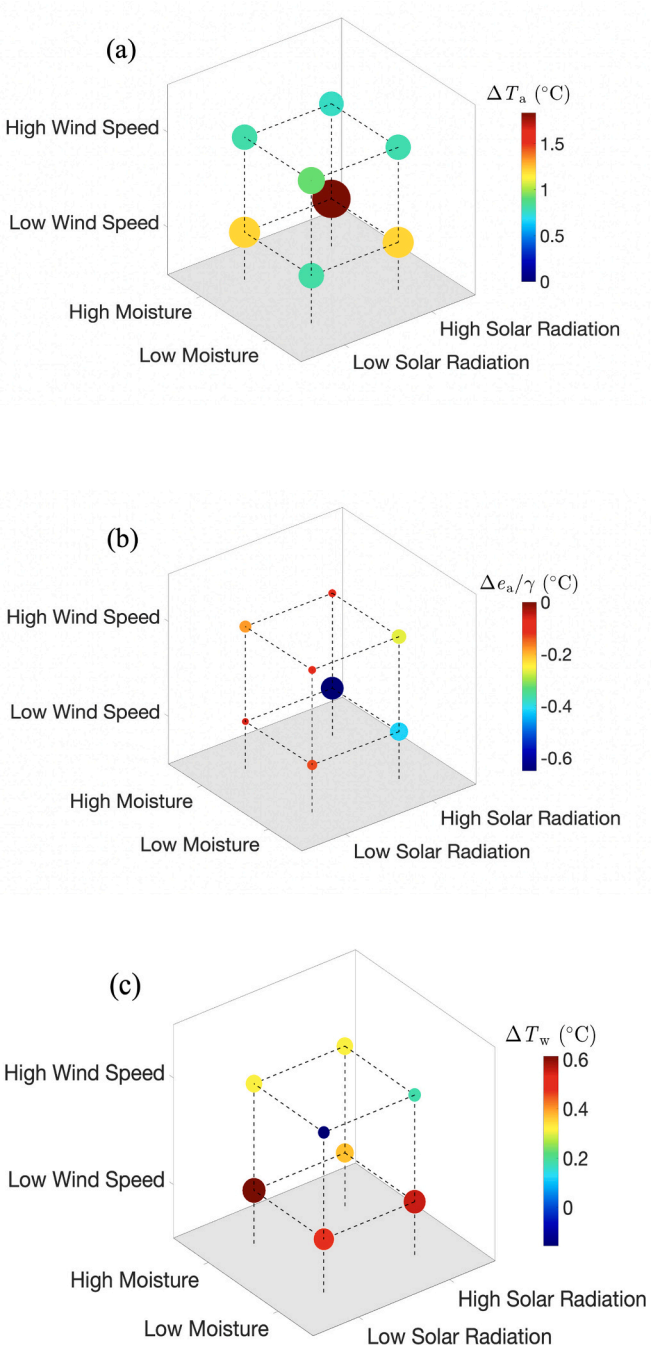

Fig. 9. Influence of weather on daytime microclimate conditions of highly built-up grids (81 sampling grids with IMP $\geq$ 90 %): (a) temperature, (b) humidity, and (c) wet-bulb temperature. Color indicates raw value and symbol size indicates deviation from zero (absolute value).

neighborhoods is slightly lower than the rural reference neighborhood ($\Delta T_w = -0.16$ °C).

At night, the highly built-up grids are warmer ($\Delta T_a > 0$) and are more humid ($\Delta e_a/\gamma > 0$), and have a greater intensity of humid heat ($\Delta T_w > 0$) than the rural reference neighborhood for all the four weather scenarios (Fig. 10). Reductions in wind speed and in soil moisture increase both temperature and humidity in these grids (Fig. 10a and 10b). As a result, the greatest increase in humid heat occurs under the low wind speed and dry soil conditions ($\Delta T_w = 1.50$ °C).

4. Discussion

4.1. Comparison with published results on intra-city variations

In the present study, the daytime temperature averaged across all seasons varies spatially across the city by 2.1 °C (maximum minus minimum). The corresponding warm season and cold season ranges are 3.0 °C and 1.4 °C, respectively. These values fall within the range of intra-city variations in temperature (0.5 to 3.5 °C) reported by a body of earlier studies (Busato et al., 2014; Deosthali, 2000; Johnson et al., 2020; Jonsson, 2004; Saaroni et al., 2000; Shi and Zhang, 2022; Unger et al., 2001; Wang et al., 2017; Winkler et al., 1981; Yan et al., 2014; Yang et al., 2020a). The all-season mean nighttime temperature variation in this study is 3.1 °C (maximum minus minimum), with the warm season range of 3.1 °C and the cold season range of 2.9 °C, again falling with the previously reported ranges (1.2 to 6.0 °C). These observed temperature variations are attributed to the elevated temperature in built-up neighborhoods relative to rural areas, conforming to the broad presence of the urban heat island phenomenon. Similar to the current study, the stronger temperature variation at night than in the day was observed in Padua, Italy (Busato et al., 2014), Tel Avia, Israel (Saaroni et al., 2000), Beijing, China (Wang et al., 2017; Yan et al., 2014), Nanjing, China (Yang et al., 2020a), and Guangzhou, China (Shi and Zhang, 2022). Observations spanning multiple seasons are in agreement with our findings that the intra-city variation in temperature is more pronounced in the warm seasons than in the cold season, both during the day (Wang et al., 2017; Yan et al., 2014) and at night (Unger et al., 2001; Winkler et al., 1981). An exception is Beijing, China, where the nighttime temperature variation is stronger in the cold season than in the warm season (Wang et al., 2017; Yan et al., 2014). This discrepancy could be explained by the greater release of anthropogenic heat in the winter than in summer, owing to space heating in this densely populated megacity. New Haven is a smaller city and is presumed to release a lower amount of anthropogenic heat than Beijing. The earlier studies suggest spatial variations in temperature are reduced with increase in wind speed and in cloudiness (Shi and Zhang, 2022; Unger et al., 2001). These patterns are also observed in the current study.

According to the data presented in a few studies on intra-city variations in humidity (Busato et al., 2014; Deosthali, 2000; Jonsson, 2004; Shi and Zhang, 2022; Yang et al., 2020a), the daytime humidity spatial variation, quantified here as $\Delta e_a/\gamma$, fall between 1.4 and 4.6 °C in the daytime and the between 0.8 and 8.9 °C at night. In the present study, the daytime humidity variation (maximum minus minimum) is 1.6 °C (all season), 3.1 °C (warm season) and 0.6 °C (cold season); these values are generally comparable to the results published in these studies. The nighttime variations in the present study are relatively low (maximum minus minimum; all-season: 1.3 °C; warm season: 2.4 °C; cold season: 0.8 °C). Generally, spatial variations in humidity are less predictable than in temperature. For example, in New Haven, air humidity can be either greater or lower in the built-up neighborhoods than the rural reference in the daytime in the warm season (Fig. 6a), but air temperature is almost always greater in the built-up neighborhoods. Averaged across all seasons, humidity in built-up neighborhoods in New Haven is decreased in the day, forming an urban dry island, and increased at night, forming an urban moist island (Table 1). These results are in line with the findings based on the annual observations in Nanjing, China (Yang et al., 2020a). Several studies show that the spatial variation in humidity is greater in the day than at night (Busato et al., 2014; Deosthali, 2000; Yang et al., 2020a), and is greater in the warm season than in the cold season (Yang et al., 2020a); These patterns are reproduced in New Haven (Fig. 6). The weather influence on humidity variation has rarely been studied. In Guangzhou, China, Shi and Zhang (2022) reported less spatially variable humidity in cloudy conditions than in clear-sky conditions.

Several authors have reported observations on intra-city variations in both temperature and humidity during the warm season. Using their data, we find that the T_w spatial range, i.e., maximum T_w minus minimum T_w, to be 0.6 °C and 1.6 °C in Guangzhou (Shi and Zhang, 2022), 0.5 °C and 0.8 °C in Nanjing (Yang et al., 2020a), and 1.0 °C and 0.1 °C in Padua (Busato et al., 2014) in the daytime and

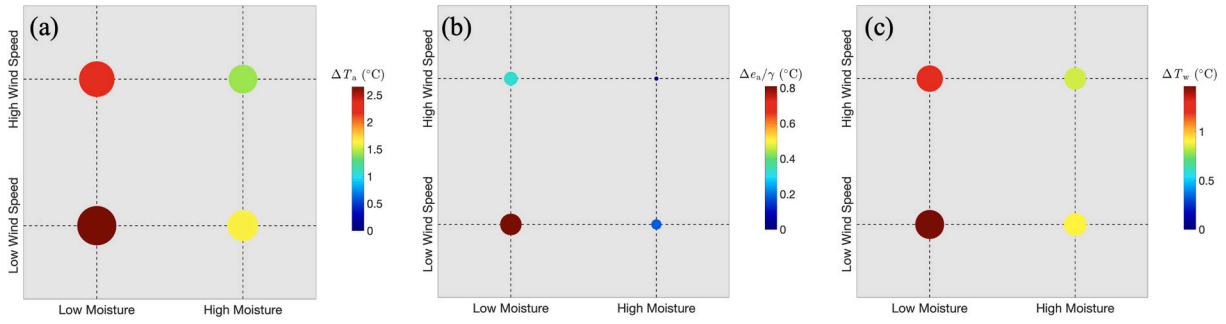

Fig. 10. Same as Fig. 9 but for nighttime.

at night, respectively. In comparison, the warm-season variation in T_w in New Haven is greater, at 1.4 °C in the daytime and 1.8 °C at night. The daytime variation in Guangzhou is associated with intensified humid heat for the built-up neighborhoods, owing to the positive contributions from the urban heat island and the urban moist island. The daytime humid heat is elevated in most built-up neighborhoods in New Haven (Supplementary Fig. 6c), and is elevated in only a few neighborhoods in Nanjing (Heavy Industry; Supplementary Fig. 9).

4.2. Mechanisms underlying the urban effects

The negative correlation between humidity and temperature spatial variations during the day (Fig. 6a and b) is indicative of evaporative effects. Evaporation reduces temperature and increases humidity. Because built-up neighborhoods have weaker evaporation sources (greenery and soil) than the rural reference, they should experience higher temperatures or urban warming effect, and lower humidity or the urban drying effect. Evaporation is affected by water and energy availability. With ample soil water and strong solar radiation, the rural vegetation evaporates water at high rates, so relatively speaking, the warming effect and drying effect in the built-up neighborhoods are enhanced (Fig. 9a and b). If either soil water or energy is limited, the spatial variations in temperature and humidity are attenuated.

A surprising result is that the correlation between humidity and temperature spatial variations is positive at night (Fig. 6c and d). In other words, a stronger urban warming effect is accompanied by a greater urban humidification. It appears that the nighttime release of heat stored in built-up neighborhoods increases the near-surface air temperature and also allows more evaporation compared to the rural land where the rate of heat storage is low. Both the increases in temperature and humidity are amplified in the dry-soil conditions compared to the wet-soil conditions (Fig. 10a and b). This is because the rural soil has a lower heat storage rate when it is drier (Spronken-Smith and Oke, 1998).

Our results suggest that dynamic mixing may be a factor in controlling the spatial variation in T_w. The evidence for this can be seen in Supplementary Fig. 10, showing that the daytime T_w decreases with increasing roughness length (z_0). In both the warm season and the cold season, T_w in the built-up neighborhoods show a prominent decreasing trend when z_0 increases. With higher surface roughness, the near surface moist static energy can dissipate more efficiently to the upper boundary layer, resulting in reduced near-surface T_w (Zhang et al., 2023). The rural neighborhoods showed high roughness and low T_w in the cold season (Supplementary Fig. 10b and 10d). They were aerodynamically smoother in the warm season (black circle in Supplementary Fig. 10a), caused by lower foliage porosity and greater plan areal fraction. The low rural T_w in the warm season possibly resulted from other diabatic processes such as the ground shading effect of tree canopies. In both seasons, Large low-rise (LCZ 8) neighborhoods were exposed to the greatest daytime T_w in the city (Supplementary Fig. 10c and 10d); there, surface roughness was low due to a mixture of fully-paved ground in parking lots and large, flat commercial buildings.

The primary mechanism for the nighttime T_w spatial variation seems to be the release of heat storage or a source of diabatic heating (Zhang et al., 2023). The nighttime T_w is found to increase with increasing building volume across the city (Supplementary Fig. 11) and with decreasing soil moisture over time (Fig. 10c). Both high building volume and low soil moisture can be regarded as indicative of increasing heat storage in built-up neighborhoods relative to the rural soil.

4.3. Implication for environmental equity

The mobile measurements provide an opportunity to investigate the heat exposure of people from various socioeconomic backgrounds and ethnic groups. For example, the wet-bulb temperature shows negative correlation with median household income during the day (Fig. 11a) and at night (Fig. 11b), indicating a disparity of heat risk among people at different socioeconomic statuses. Using the best-fit functions, we found the lowest income group (20,000–25,000 USD per year) experiences a greater humid heat than the highest income group (120,000–125,000 USD per year); the difference is 0.24 °C in the daytime and 0.45 °C at night. The positive correlation between ΔT_w and percent of people of color (Fig. 11c and d) shows that people of color (Black, Hispanic, Asian, and American Indian) may be subject to more humid heat stress than the non-Hispanic White population. The disparity between non-White (percent of POC = 100 %) and White communities (percent of POC = 0 %) is relatively weak (0.08 °C) in the day but is observable at night (0.35 °C). These disparities also exist across seasons (Supplementary Fig. 12 and 13).

4.4. Implications for heat risk and adaptation strategies

A wet-bulb temperature of 27 °C has been widely regarded as a threshold beyond which human mortality increases significantly (Im et al., 2017; Zhang et al., 2023). Long-term records from the local weather station in New Haven (red triangle in Fig. 1) indicate six exposure days (daily maximum $T_w > 27$ °C) over the past decade. Compared to the station, built-up neighborhoods can increase daytime mean T_w by up to 0.80 °C in the warm season. By adding this increment to the historical station records, the number of exposure days rises to ten days per decade, underscoring the sensitivity of a statistical distribution's tails to the mean change. Climate modeling results (Coffel et al., 2017) suggest that the mean daily maximum T_w in the coastal region of Northeast US should increase by approximately 1.5 °C from the last decade to the period 2060–2080 under the RCP8.5 scenario. By shifting the observed T_w probability distribution by the sum of this climate warming signal and the urban effect, the number of exposure days would increase to 70 days per decade in the built-up neighborhoods in New Haven.

Humans need to adapt to an increasingly warmer and more humid climate (Coffel et al., 2017; Willett et al., 2007). Based on the

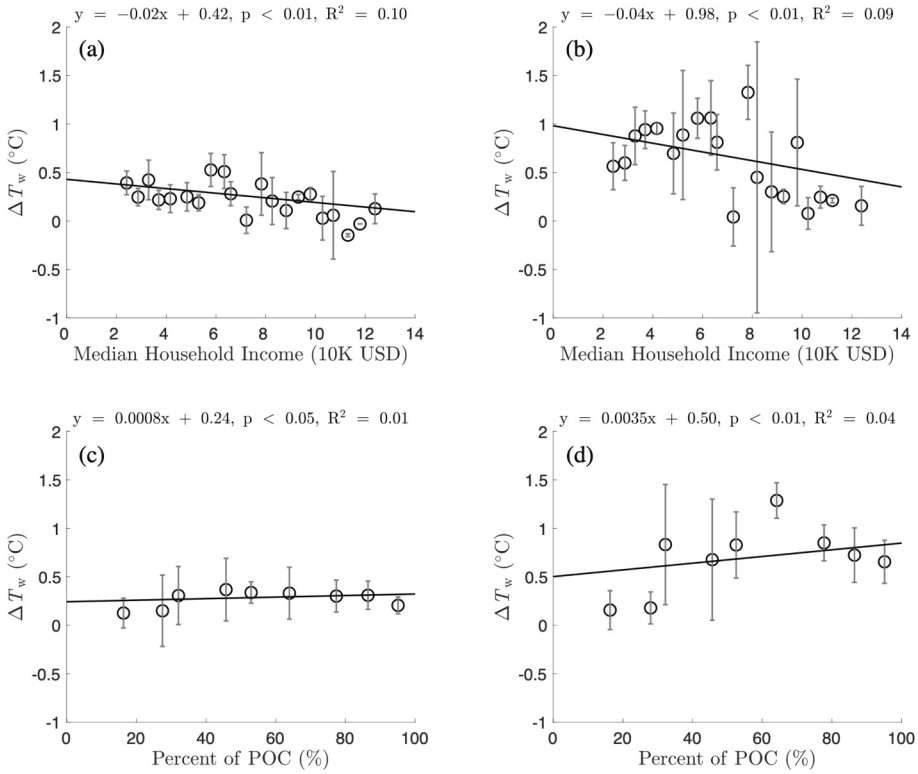

Fig. 11. Relationship between all-season mean wet-bulb temperature change (ΔT_w) and median household income (a and b) and percent of people of color (c and d). (a) and (c) are daytime results and (b) and (d) are for nighttime results. Circles are bin averages (bin size $5000 in a and b and 10 % in c and d). Error bars are ±1 standard deviation. The back lines are best-fit functions derived from original data.

findings of this study, local strategies to mitigate humid heat includes adjusting building morphology for promoting heat dissipation, optimizing building materials to reduce heat storage, and using reflective coatings to lower the absorption of radiative energy. Urban greenspaces can mitigate nighttime humid heat by reducing diabatic heating, but they may not be as effective in the daytime due to increased humidity from evaporation.

This study focuses on humid heat, or the combined effect of temperature and humidity on human thermal comfort. It omits other meteorological factors like wind condition and solar radiation, which can also affect human heat stress (Höppe, 1999; Jendritzky et al., 2012). Another limitation is that wet-bulb temperature sets a strong assumption that the human body cools its skin only via evaporating sweat (Sherwood and Huber, 2010). To approach the wet-bulb temperature, the body must be well-hydrated and in a well-ventilated environment. These conditions are not always fulfilled in practice. In this regard, the wet-bulb temperature may underestimate the true heat stress.

5. Conclusions

In this study, we investigated the intra-city variation in humid heat using data collected via a mobile smart sensor in a mid-latitude city. The main novelty lies in the use of the wet-bulb equation as a measure of humid heat to isolate the contributions from temperature and humidity. Additionally, the mobile measurements produced information on spatial variations in humid heat with a high spatial resolution and under all-weather conditions that have rarely been achieved in earlier research. The key findings are summarized as follows:

(1) The spatial variation in humid heat was controlled by the degree of development; the greatest humid heat occurred in neighborhoods with the highest imperviousness and the lowest vegetation cover. These neighborhoods were home to communities of low-income and people of color.
(2) There is a resemblance between the intra-city variations in air temperature and in land surface temperature, but land surface temperature exaggerated the disparity in heat exposure by approximately ninefold as opposed to air temperature.
(3) The spatial variation in humid heat was stronger at night than during the day. The nighttime variation in humid heat was greater in the cold season than in the warm season. The highly built-up neighborhoods in the city experienced the most elevated humid heat in the cold-season nights, with an average increase of 1.20 °C in wet-bulb temperature relative to the rural reference neighborhood.

(4) Weather exerted a strong influence on the spatial variation in humid heat. In the highly built-up neighborhoods, the largest increase in the daytime humid heat (relative to the rural reference) occurred under the conditions of weak wind, low solar radiation and high soil moisture. At night, these neighborhoods experienced the greatest humid heat in the weak-wind and dry-soil conditions.
(5) Intracity variations in humid heat were contributed more by temperature variations than by the humidity variations. In the daytime, temperature and humidity were negatively correlated across space, that is, high-temperature neighborhoods generally had lower air humidity. At night, the two variables were positively correlated: warmer neighborhoods were more humid.

Code availability

The MATLAB code used to preprocess data and to produce the figures in this paper is available at https://figshare.com/s/4aa0082ec204b83e86e5.

Author contributions

X.L. designed the research. Y.Y. designed the methods and collected the data. X.L. and Y.Y. analyzed the data and drafted the manuscript.

CRediT authorship contribution statement

Yichen Yang: Writing – original draft, Visualization, Validation, Software, Methodology, Investigation, Formal analysis, Data curation. **Xuhui Lee:** Writing – review & editing, Validation, Supervision, Resources, Project administration, Investigation, Funding acquisition, Conceptualization.

Declaration of competing interest

The authors declare that they have no known competing financial interests or personal relationships that could have appeared to influence the work reported in this paper.

Data availability

The mobile ensemble data is available at: https://figshare.com/s/4aa0082ec204b83e86e5. The impervious surface fraction (IMP) data is available at https://www.usgs.gov/centers/eros/science/national-land-cover-database. The Landsat land surface temperature products are open to download at https://earthexplorer.usgs.gov. For urban morphology, the GLAMOUR dataset is provided at https://zenodo.org/records/10396451. The ESA WorldCover land use data was published at https://esa-worldcover.org/en. The Global Forest Canopy Height 2019 dataset can be downloaded via https://glad.umd.edu/dataset/gedi. Finally, the census tabular data for heat disparity assessment is from https://www.census.gov/programs-surveys/acs/data.html.

Acknowledgements

X.L. acknowledges support by the Robert Wood Johnson Foundation (grant 77476), and Y.Y. by a Yale Graduate Fellowship. We thank Chang Cao for testing the mobile measurement system in the early stage of development, and Randall Semagin, Paul E Farrell, and Peter Babich for providing stationary monitoring data of New Haven.

Appendix A. Supplementary data

Supplementary data to this article can be found online at https://doi.org/10.1016/j.uclim.2024.102201.

References

Busato, F., Lazzarin, R.M., Noro, M., 2014. Three years of study of the urban Heat Island in Padua: experimental results. Sustain. Cities Soc. 10, 251–258.
Cao, C., Yang, Y., Lu, Y., Schultze, N., Gu, P., Zhou, Q., Xu, J., Lee, X., 2020. Performance evaluation of a smart mobile air temperature and humidity sensor for characterizing intracity thermal environment. J. Atmos. Ocean. Technol. 37 (10), 1891–1905.
Chakraborty, T., Hsu, A., Manya, D., Sheriff, G., 2019. Disproportionately higher exposure to urban heat in lower-income neighborhoods: a multi-city perspective. Environ. Res. Lett. 14 (10), 105003.
Chakraborty, T., Newman, A.J., Qian, Y., Hsu, A., Sheriff, G., 2023. Residential segregation and outdoor urban moist heat stress disparities in the United States. One Earth 6 (6), 738–750.
Cilek, M.U., Cilek, A., 2021. Analyses of land surface temperature (LST) variability among local climate zones (LCZs) comparing Landsat-8 and ENVI-met model data. Sustain. Cities Soc. 69, 102877.
Coffel, E.D., Horton, R.M., De Sherbinin, A., 2017. Temperature and humidity based projections of a rapid rise in global heat stress exposure during the 21st century. Environ. Res. Lett. 13 (1), 014001.

Daramola, M.T., Balogun, I.A., 2019. Analysis of the urban surface thermal condition based on sky-view factor and vegetation cover. Remote Sens. Appl.: Soc. Environ. 15, 100253.
Demuzere, M., Hankey, S., Mills, G., Zhang, W., Lu, T., Bechtel, B., 2020. Combining expert and crowd-sourced training data to map urban form and functions for the continental US. Sci. data 7 (1), 264.
Demuzere, M., Kittner, J., Bechtel, B., 2021. LCZ generator: a web application to create local climate zone maps. Front. Environ. Sci. 9, 637455.
Demuzere, M., Kittner, J., Martilli, A., Mills, G., Moede, C., Stewart, I.D., Van Vliet, J., Bechtel, B., 2022. A global map of local climate zones to support earth system modelling and urban scale environmental science. Earth Syst. Sci. Data Discuss. 2022, 1–57.
Deosthali, V., 2000. Impact of rapid urban growth on heat and moisture islands in Pune City, India. Atmos. Environ. 34 (17), 2745–2754.
Economic, U. D. O., & Affairs, S, 2018. World Urbanization Prospects: 2018 Revision. Key Facts.
Grimmond, C., Oke, T.R., 1999. Aerodynamic properties of urban areas derived from analysis of surface form. J. Appl. Meteorol. Climatol. 38 (9), 1262–1292.
Höppe, P., 1999. The physiological equivalent temperature–a universal index for the biometeorological assessment of the thermal environment. Int. J. Biometeorol. 43, 71–75.
Hsu, A., Sheriff, G., Chakraborty, T., Manya, D., 2021. Disproportionate exposure to urban heat island intensity across major US cities. Nat. Commun. 12 (1), 2721.
Im, E.-S., Pal, J.S., Eltahir, E.A., 2017. Deadly heat waves projected in the densely populated agricultural regions of South Asia. Sci. Adv. 3 (8), e1603322.
Jendritzky, G., de Dear, R., Havenith, G., 2012. UTCI—why another thermal index? Int. J. Biometeorol. 56, 421–428.
Johnson, S., Ross, Z., Kheirbek, I., Ito, K., 2020. Characterization of intra-urban spatial variation in observed summer ambient temperature from the new York City Community air survey. Urban Clim. 31, 100583.
Jonsson, P., 2004. Vegetation as an urban climate control in the subtropical city of Gaborone, Botswana. Int. J. Climatol. 24 (10), 1307–1322.
Koc, C.B., Osmond, P., Peters, A., Irger, M., 2018. Understanding land surface temperature differences of local climate zones based on airborne remote sensing data. IEEE J. Selected Topics Appl. Earth Observ. Remote Sens. 11 (8), 2724–2730.
Köppen, W., 1900. Versuch einer Klassifikation der Klimate, vorzugsweise nach ihren Beziehungen zur Pflanzenwelt. Geogr. Z. 6 (11. H), 593–611.
Kuang, W., Liu, Y., Dou, Y., Chi, W., Chen, G., Gao, C., Yang, T., Liu, J., Zhang, R., 2015. What are hot and what are not in an urban landscape: quantifying and explaining the land surface temperature pattern in Beijing, China. Landsc. Ecol. 30, 357–373.
Li, R., Sun, T., Ghaffarian, S., Tsamados, M., Ni, G., 2024. GLAMOUR: GLobAl building MOrphology dataset for URban hydroclimate modelling. Sci. data 11 (1), 618.
Logan, T., Zaitchik, B., Guikema, S., Nisbet, A., 2020. Night and day: the influence and relative importance of urban characteristics on remotely sensed land surface temperature. Remote Sens. Environ. 247, 111861.
Nichol, J.E., Wong, M.S., 2008. Spatial variability of air temperature and appropriate resolution for satellite-derived air temperature estimation. Int. J. Remote Sens. 29 (24), 7213–7223.
Noro, M., Busato, F., Lazzarin, R., 2015. Urban heat island in Padua, Italy: experimental and theoretical analysis. Indoor and Built Environ. 24 (4), 514–533.
Oke, T.R., 1981. Canyon geometry and the nocturnal urban heat island: comparison of scale model and field observations. J. Climatol. 1 (3), 237–254.
Oke, T.R., 1982. The energetic basis of the urban heat island. Q. J. R. Meteorol. Soc. 108 (455), 1–24.
Potapov, P., Li, X., Hernandez-Serna, A., Tyukavina, A., Hansen, M.C., Kommareddy, A., Pickens, A., Turubanova, S., Tang, H., Silva, C.E., 2021. Mapping global forest canopy height through integration of GEDI and Landsat data. Remote Sens. Environ. 253, 112165.
Saaroni, H., Ben-Dor, E., Bitan, A., Potchter, O., 2000. Spatial distribution and microscale characteristics of the urban heat island in Tel-Aviv, Israel. Landscape and urban planning 48 (1–2), 1–18.
Sherwood, S.C., Huber, M., 2010. An adaptability limit to climate change due to heat stress. Proc. Natl. Acad. Sci. 107 (21), 9552–9555.
Shi, Y., Zhang, Y., 2022. Urban morphological indicators of urban heat and moisture islands under various sky conditions in a humid subtropical region. Build. Environ. 214, 108906.
Spronken-Smith, R., Oke, T., 1998. The thermal regime of urban parks in two cities with different summer climates. Int. J. Remote Sens. 19 (11), 2085–2104.
Stewart, I.D., 2011. A systematic review and scientific critique of methodology in modern urban heat island literature. Int. J. Climatol. 31 (2), 200–217.
Tran, D.X., Pla, F., Latorre-Carmona, P., Myint, S.W., Caetano, M., Kieu, H.V., 2017. Characterizing the relationship between land use land cover change and land surface temperature. ISPRS J. Photogramm. Remote Sens. 124, 119–132.
Unger, J., Sümeghy, Z., Zoboki, J., 2001. Temperature cross-section features in an urban area. Atmos. Res. 58 (2), 117–127.
Wang, K., Jiang, S., Wang, J., Zhou, C., Wang, X., Lee, X., 2017. Comparing the diurnal and seasonal variabilities of atmospheric and surface urban heat islands based on the Beijing urban meteorological network. J. Geophys. Res. Atmos. 122 (4), 2131–2154.
Waugh, D.W., Zaitchik, B., Scott, A.A., Ibsen, P.C., Jenerette, G.D., Schatz, J., Kucharik, C.J., 2023. Limited role of absolute humidity in Intraurban heat variability. J. Appl. Meteorol. Climatol. 62 (12), 1845–1854.
Willett, K.M., Gillett, N.P., Jones, P.D., Thorne, P.W., 2007. Attribution of observed surface humidity changes to human influence. Nature 449 (7163), 710–712.
Winkler, J.A., Skaggs, R.H., Baker, D.G., 1981. Effect of temperature adjustments on the Minneapolis-St. Paul urban heat island. J. Appl. Meteorol. Climatol. 20 (11), 1295–1300.
Yan, H., Fan, S., Guo, C., Hu, J., Dong, L., 2014. Quantifying the impact of land cover composition on intra-urban air temperature variations at a mid-latitude city. PLoS One 9 (7), e102124.
Yang, Y., Lee, X., 2022. A scale-separating framework for fusing satellite land surface temperature products. Remote Sens. 14 (4), 983.
Yang, X., Peng, L.L., Chen, Y., Yao, L., Wang, Q., 2020a. Air humidity characteristics of local climate zones: a three-year observational study in Nanjing. Build. Environ. 171, 106661.
Yang, G., Yu, Z., Jørgensen, G., Vejre, H., 2020b. How can urban blue-green space be planned for climate adaption in high-latitude cities? A seasonal perspective. Sustain. Cities Soc. 53, 101932.
Yang, Y., Cao, C., Bogoev, I., Deetman, C., Dietz, G., Hang, J., Howard, L., Huang, X., Kendall, N., Lai, J., Lam, H., Tam, K., Yoo, C., Zhang, K., Lee, X., 2024. Regulation of humid heat by urban greenspace across a climate wetness gradient. Nature Cities. https://doi.org/10.1038/s44284-024-00157-y.
Yu, Z., Guo, X., Jørgensen, G., Vejre, H., 2017. How can urban green spaces be planned for climate adaptation in subtropical cities? Ecol. Indic. 82, 152–162.
Yu, Z., Xu, S., Zhang, Y., Jørgensen, G., Vejre, H., 2018. Strong contributions of local background climate to the cooling effect of urban green vegetation. Sci. Rep. 8 (1), 6798.
Yu, K., Chen, Y., Wang, D., Chen, Z., Gong, A., Li, J., 2019. Study of the seasonal effect of building shadows on urban land surface temperatures based on remote sensing data. Remote Sens. 11 (5), 497.
Zhang, K., Cao, C., Chu, H., Zhao, L., Zhao, J., Lee, X., 2023. Increased heat risk in wet climate induced by urban humid heat. Nature 1–5.

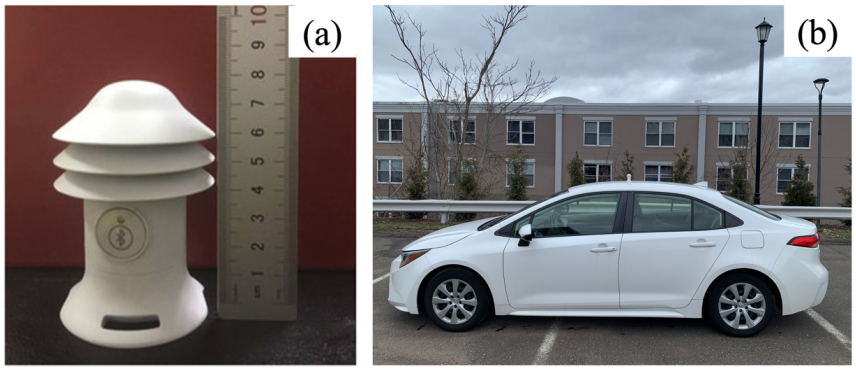

Supplementary Figure 1. Photos of (a) Smart-T sensor and (b) the sensor attached to the roof of a white passenger car.

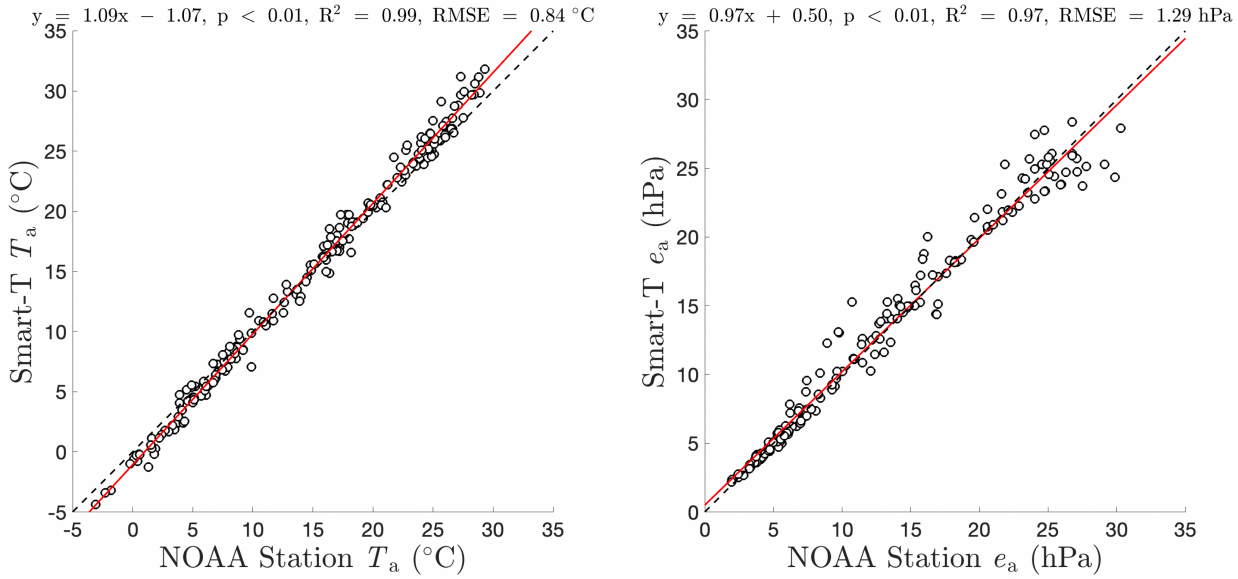

(a) (b)

Supplementary Figure 2. Relationship between Smart-T and the NOAA station for (1) air temperature T_a and (2) water vapor pressure e_a. Measurements were made near the station at the beginning and the end of each trip. Each data point represents a one-minute average. Red solid lines show the linear regression functions. Black dashed lines indicate 1:1 relationship.

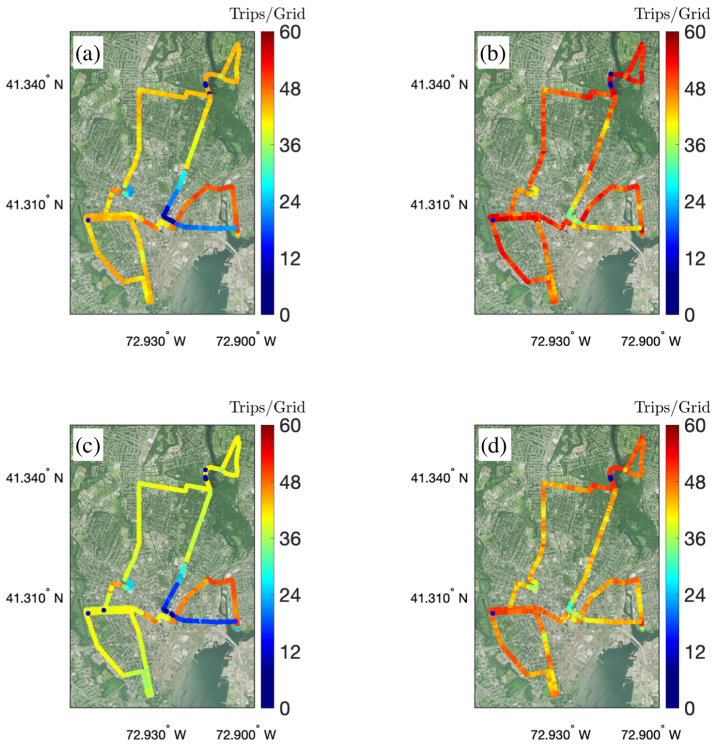

Supplementary Figure 3. Number of trips in each ensemble sampling grid for (a) daytime in the warm season, (b) daytime in the cold season, (c) nighttime in the warm season, and (d) nighttime in the cold season. Trip overlap can be low due to occasional failure in data logging and road blockage.

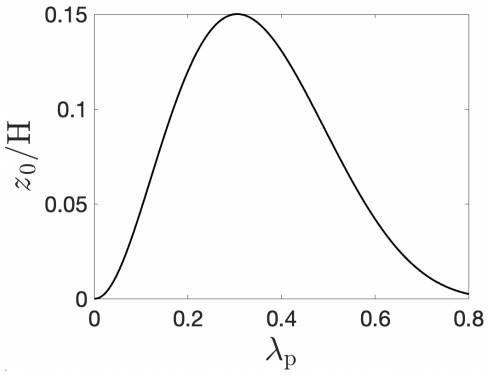

Supplementary Figure 4. The ratio of roughness length to height as a function of plan areal fraction. This figure is adapted from Figure 1a in Grimmond and Oke (1999).

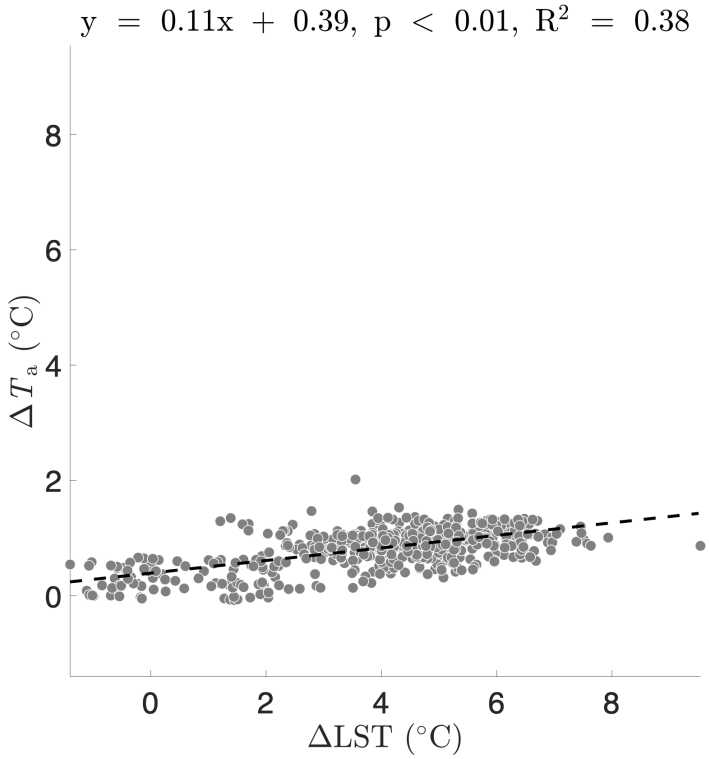

Supplementary Figure 5. Relationship between air temperature change and land surface temperature change across the city. Each data point represents the all-season average at one sampling grid.

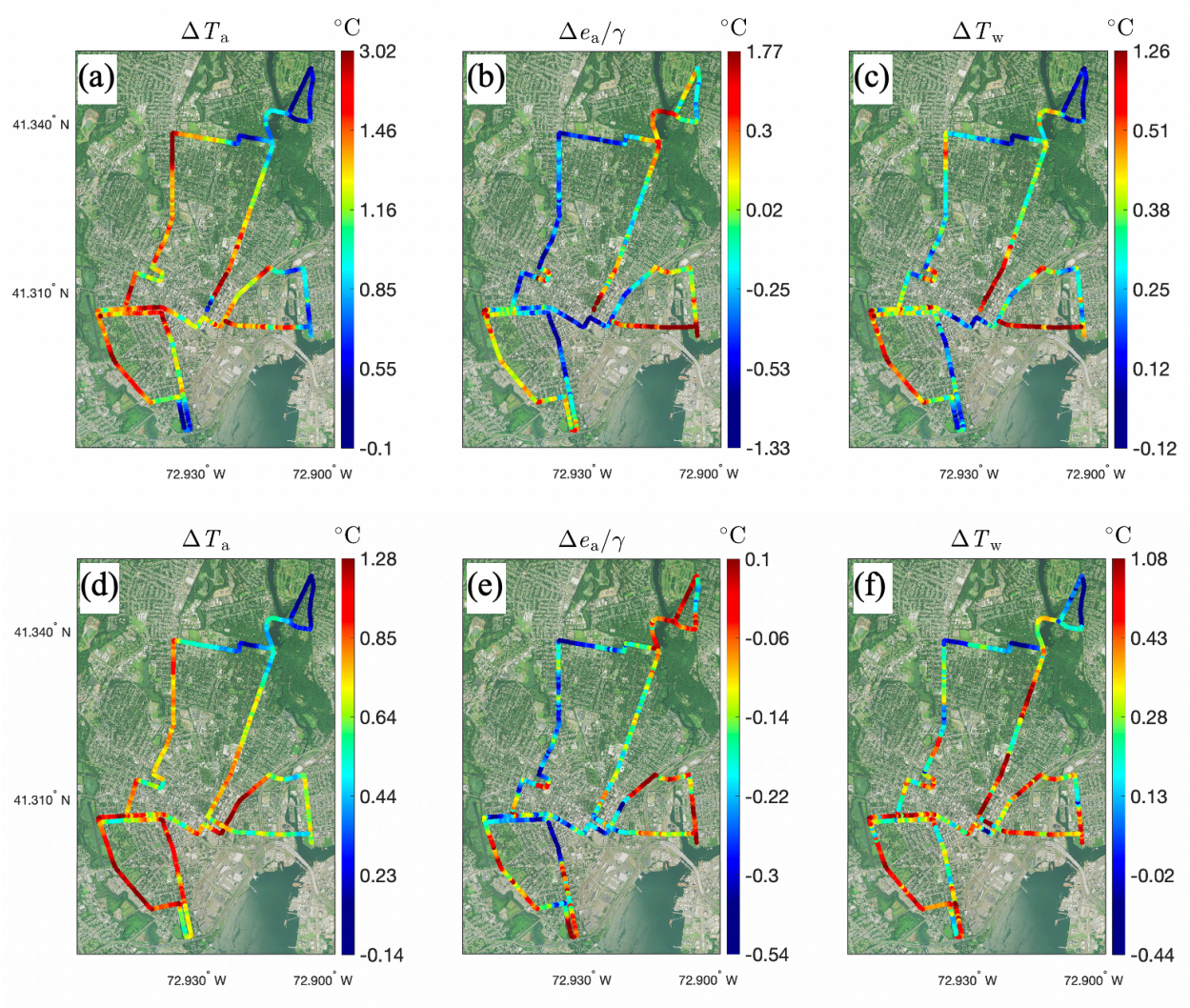

Supplementary Figure 6. Ensemble maps of daytime variations in air temperature (ΔT_a), humidity ($\Delta e_a/\gamma$), and in wet-bulb temperature (ΔT_w) for the warm season (a, b, and c) and the cold season (d, e, and f).

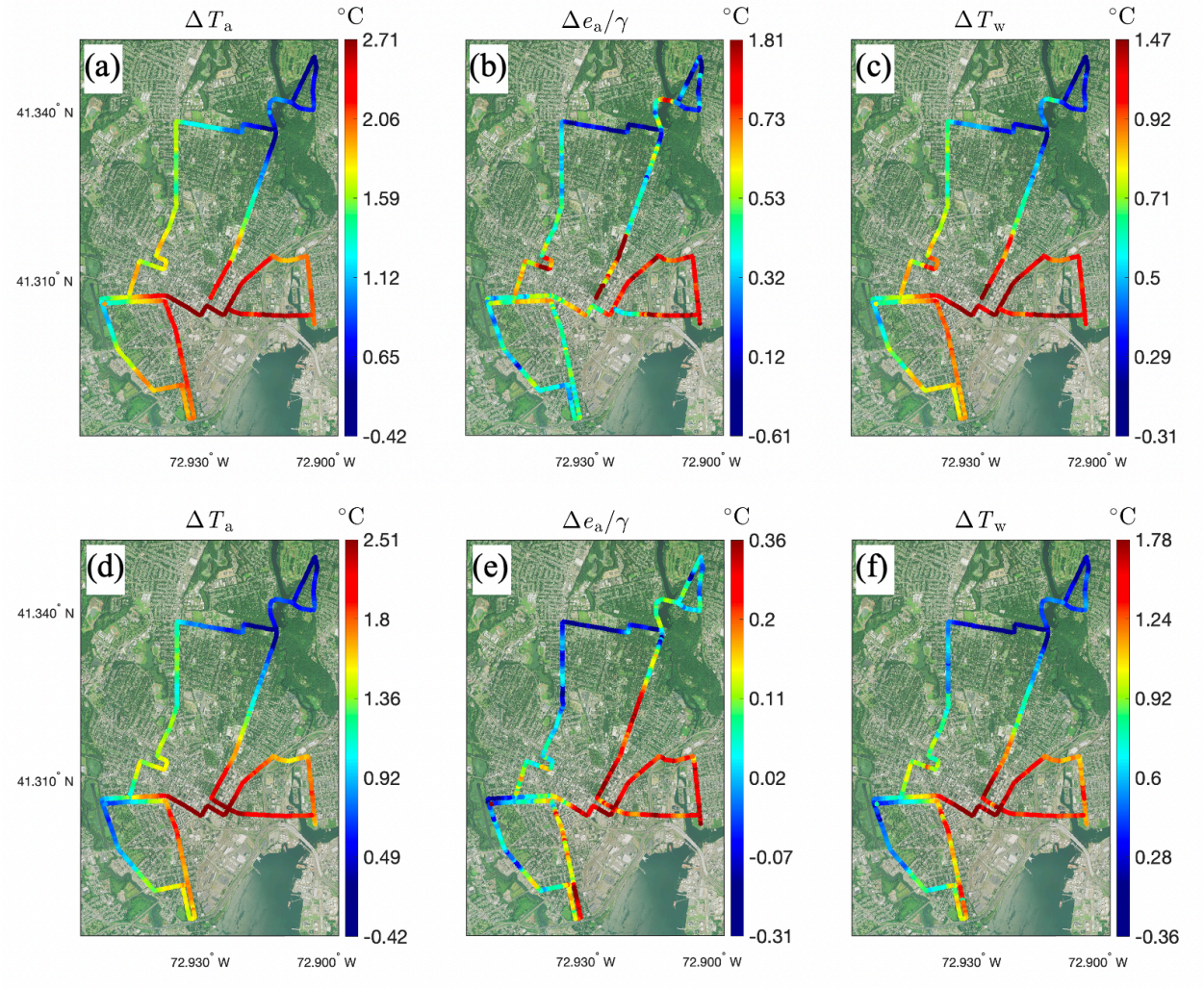

Supplementary Figure 7. Ensemble maps of nighttime variations in air temperature (ΔT_a), humidity ($\Delta e_a/\gamma$), and wet-bulb temperature (ΔT_w) for the warm season (a, b, and c) and the cold season (d, e, and f).

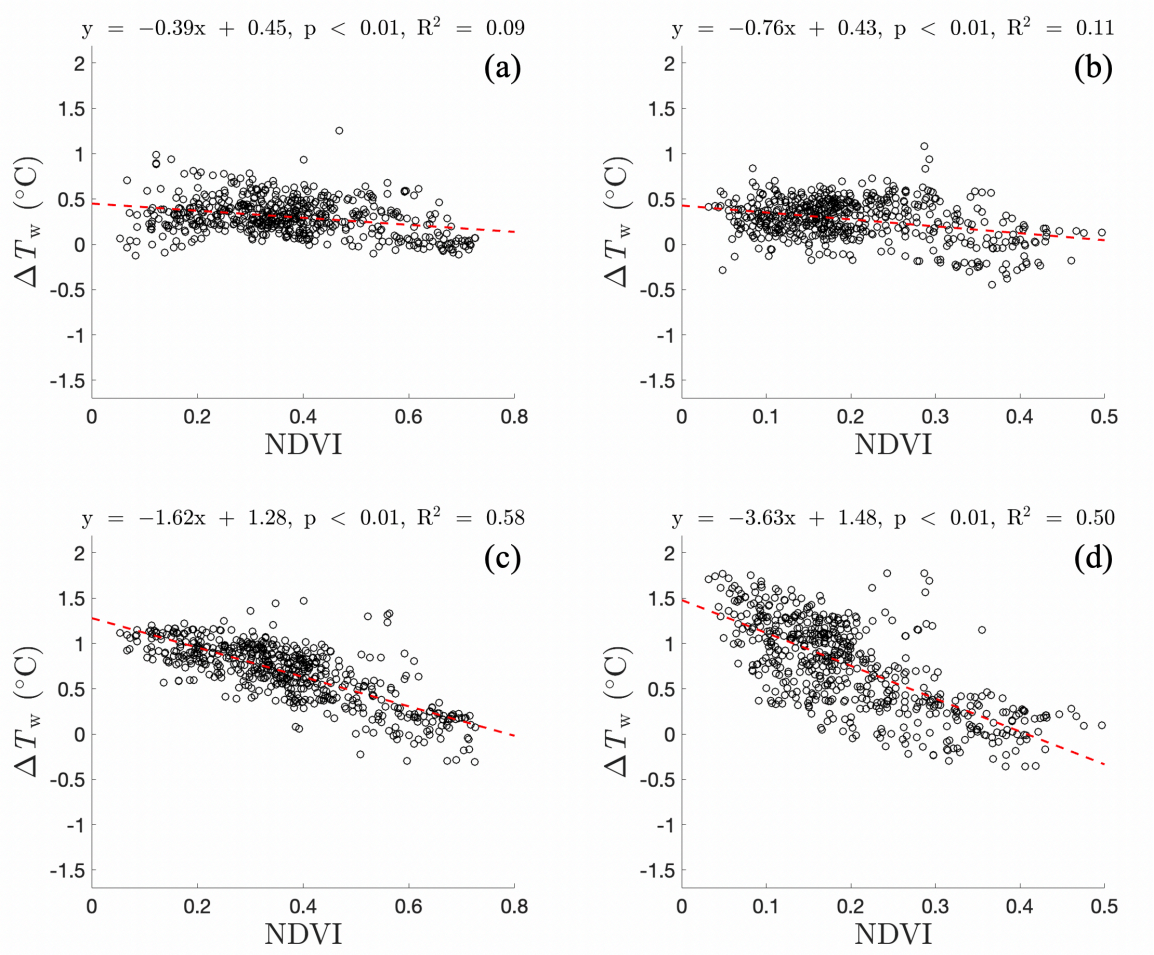

Supplementary Figure 8. Relationship between NDVI and wet-bulb temperature (ΔT_w) in (a) the daytime in the warm season, (b) the daytime in the cold season, (c) the nighttime in the warm season, and (d) the nighttime in the cold season. Red lines display the best-fitting functions. Each datapoint represents one sampling grid.

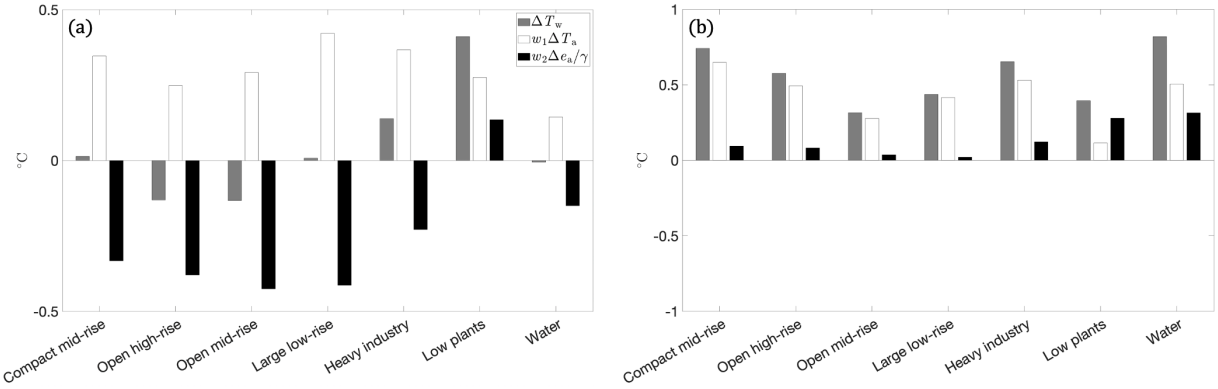

Supplementary Figure 9. Wet-bulb temperature change (ΔT_w) and its temperature ($w_1 \Delta T_a$) and humidity component ($w_2 \Delta e_a/\gamma$) in difference local climate zones in Nanjing, China, in (a) daytime and (b) nighttime. Results are for the warm season. All the changes are relative to observations in LCZ A (Dense Trees). Data source: X. Yang et al. (2020).

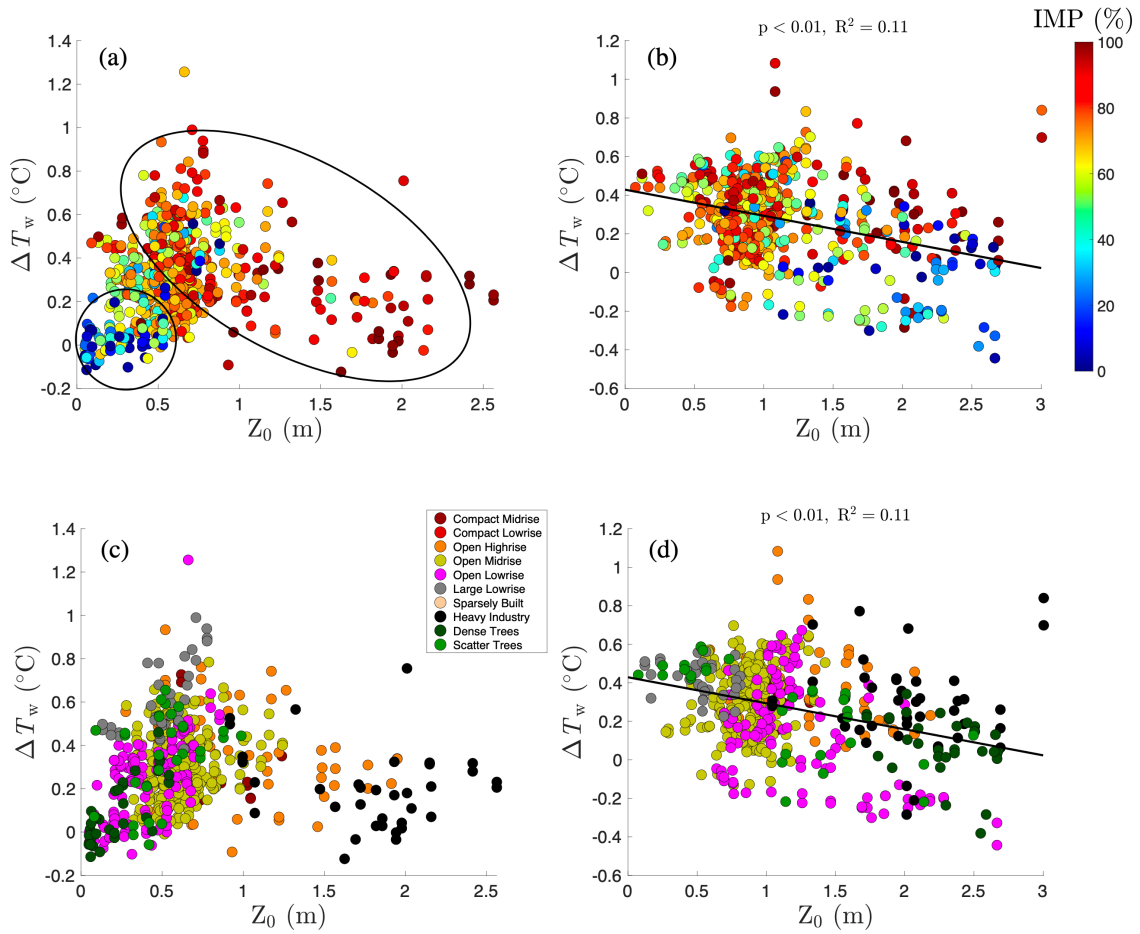

Supplementary Figure 10. Relationship between change in the daytime wet-bulb temperature (ΔT_w) and roughness length in the warm season (a and c) and the cold season (b and d). Each data point is an aggregate within 150-radius from an ensemble sampling grid. Color indicates impervious surface fraction in (a) and (b), and local climate zone in (c) and (d). The oval in (a) marks the built-up neighborhoods, and the circle indicates the rural neighborhoods. Black lines in (b) and (d) show the best-fit linear functions between ΔT_w and z_0. Local climate zone data source: Demuzere et al., 2022;

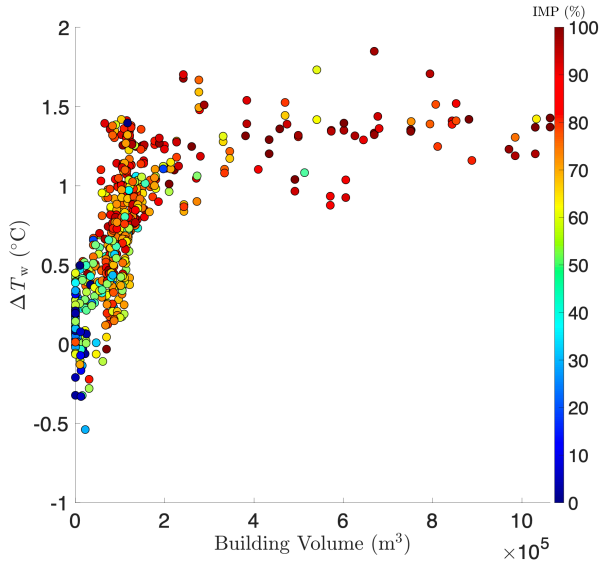

Supplementary Figure 11. Relationship between change in the nighttime wet-bulb temperature (ΔT_w) and building volume. Color indicates impervious surface fraction (IMP). Building volume was computed from the GLAMOUR dataset (Li et al., 2024) at 100-m resolution and aggregated within 150-radius from an ensemble sampling grid.

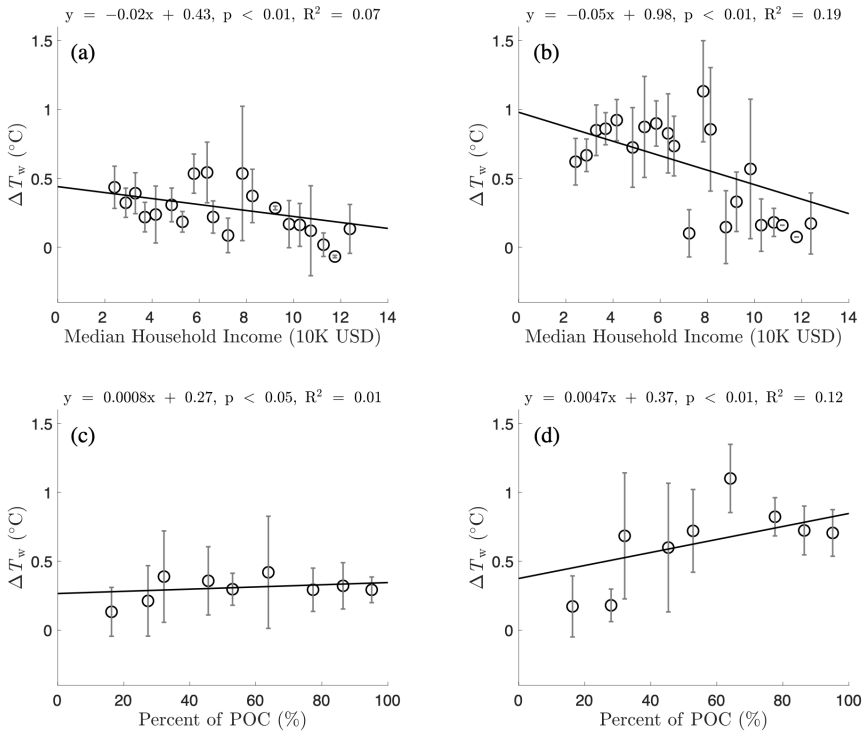

Supplementary Figure 12. Relationship between wet-bulb temperature change (ΔT_w) and median household income (a and b) and percent of people of color (c and d) during the warm season. (a) and (c) are daytime results and (b) and (d) are nighttime results.

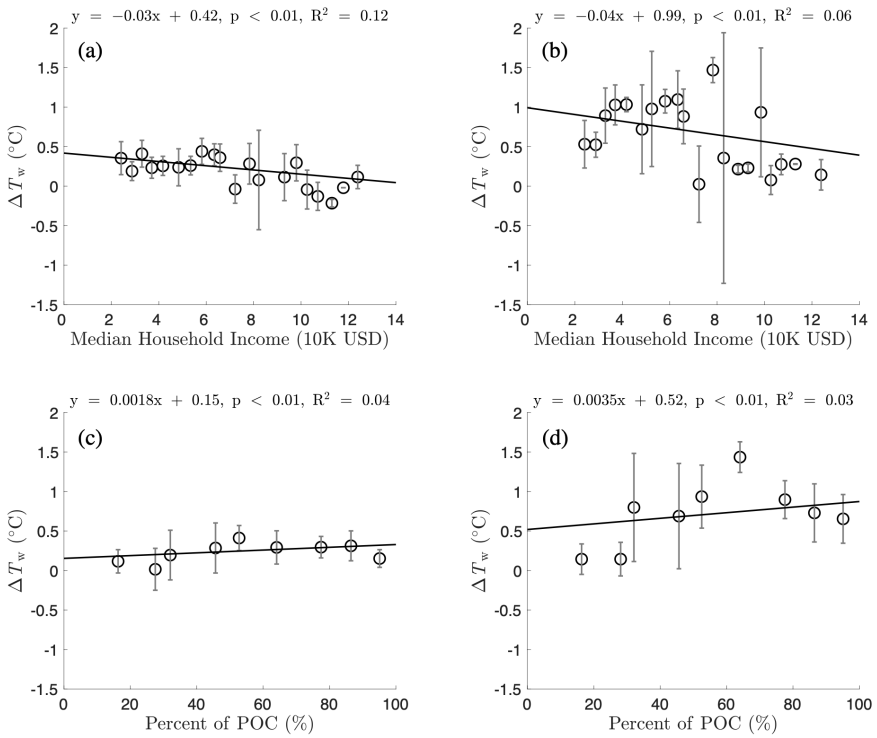

Supplementary Figure 13. Relationship between wet-bulb temperature change (ΔT_w) and median household income (a and b) and percent of people of color (c and d) during the cold season. (a) and (c) are daytime results and (b) and (d) are nighttime results.